Cover Letter

Modeling Reactive Multi-Component Multi-Phase Flow for Geological Carbon Sequestration (GCS) with Matlab

Yufei Wang,Daniel Fernàndez-Garcia,Maarten W. Saaltink

Dear Editors-in-Chief,

Please find the enclosed manuscript "Modeling Reactive Multi-Component Multi-Phase Flow for Geological Carbon Sequestration (GCS) with Matlab", which we are submitting for exclusive consideration for publication in Computers & Geosciences. We confirm that the submission follows all the requirements and includes all the items of the submission checklist.

The manuscript presents a reactive multi-component three-phase flow model for Geological Carbon Sequestration (GCS), an efficient approach to reduce carbon emissions. This model is implemented in `MRST`, an open-source Matlab®-based platform. This model has two main features. Firstly, it considers the chemical reaction among the gas phase, the brine phase and the formation rock. Secondly, the independent variables are split into independent transport variables that describe the transport information and independent reaction variables that represent the chemical reaction information. These independent variables are solved with sequential iteration method. Finally, we give a benchmark test and an application example of this proposed program.

We provide the source codes in a public repository with details listed in the section "Code availability".

Thanks for your consideration.

Sincerely,

Yufei Wang, Daniel Fernàndez-Garcia and Maarten W. Saaltink
Corresponding author Yufei Wang through emai: yufei.wang@upc.edu

Highlights

Modeling Reactive Multi-Component Multi-Phase Flow for Geological Carbon Sequestration (GCS) with Matlab

Yufei Wang,Daniel Fernàndez-Garcia,Maarten W. Saaltink

- We offer a numerical program for simulating geological carbon sequestration;
- The program accounts for the chemical reaction among gas, liquid and rock phases;
- The chemical reaction is solved with mass action law;
- The program solves the mass transport and the chemical reaction with sequential iteration method.

Modeling Reactive Multi-Component Multi-Phase Flow for Geological Carbon Sequestration (GCS) with Matlab

Yufei Wang[a], Daniel Fernàndez-Garcia[b] and Maarten W. Saaltink[c]

[a]Dept. of Civil and Environmental Engineering. Universitat Politècnica de Catalunya, Jordi Girona 1-3, 08034 Barcelona, Spain
[a]Associated Unit: Hydrogeology Group (UPC-CSIC)
[b]Dept. of Civil and Environmental Engineering. Universitat Politècnica de Catalunya, Jordi Girona 1-3, 08034 Barcelona, Spain
[b]Associated Unit: Hydrogeology Group (UPC-CSIC)
[c]Dept. of Civil and Environmental Engineering. Universitat Politècnica de Catalunya, Jordi Girona 1-3, 08034 Barcelona, Spain
[c]Associated Unit: Hydrogeology Group (UPC-CSIC)

ARTICLE INFO

Keywords:
Geological carbon sequestration
Reactive transport
Multi-phase flow
Geochemistry

ABSTRACT

We present a reactive multi-component three-phase flow program for simulating Geological Carbon Sequestration (GCS), an approach that reduces carbon emissions by storing CO_2 in deep subsurface formations. The program, called `MRST_CO2`, is implemented in the library Matlab Reservoir Simulation Toolbox (MRST) and has two main features. Firstly, this program takes into account the flow or mass balance equations of gas, liquid and formation rock phases, which affects the transport process by giving rise to mass exchanges among phases. Secondly, the independent variables are split into independent transport variables that describe the transport information and independent reaction variables that represent the chemical reaction information. These independent variables are solved with sequential iteration method. Finally, we give a benchmark test and an application example of this proposed program.

CRediT authorship contribution statement

Yufei Wang: Modelling, writing and coding. **Daniel Fernàndez-Garcia:** Modelling, writing and supervising. **Maarten W. Saaltink:** Modelling, writing and supervising.

1. Introduction

In many fields of geological engineering, numerical modelling is an important tool for understanding geological processes, analysis of laboratory and field experiments and predicting future scenarios. An example of such a field is Geological Carbon Sequestration (GCS), which aims to mitigate carbon emissions by storing CO_2 in deep formations (Juanes et al., 2006; Xu et al., 2006; EU GeoCapacity, 2009; Vilarrasa et al., 2010a; Nordbotten and Celia, 2011; U.S. Department of Energy, 2012; Tutolo et al., 2015a; Lei et al., 2016; Liu et al., 2019). Modeling GCS is particularly challenging because it implies the interaction of brine and a CO_2-rich phase with chemical reactions, mass transport, heat transfer and mechanical rock deformations (Gaus et al., 2008). Moreover, it requires the numerical solution of a large number of coupled partial differential equations and equations of state that are highly nonlinear.

Many open-source and commercial codes have been developed for simulating GCS. Popular numerical codes that can be applied to GCS are TOUGH (Pruess et al., 1999; Xu et al., 2006; Zhang et al., 2008; Xu et al., 2011), GPRS (Cao, 2002; Jiang, 2008), CODEBRIGHT (Olivella et al., 1994, 1996), RETRASO (Saaltink et al., 2004, 2013), NUFT

ORCID(s): 0000-0002-1955-5984 (Y. Wang); 0000-0002-4667-3003 (D. Fernàndez-Garcia); 0000-0003-0553-4573 (M.W. Saaltink)

(Johnson et al., 2005; Morris et al., 2011; Hao et al., 2012), FEHM (Robinson et al., 2000), IPARS (Wheeler et al., 2007) and DUNE (Flemisch et al., 2011; Neumann et al., 2013). These codes have been used to assess the efficiencies of different trapping mechanisms (i.e., hydrodynamic, capillary, dissolution and mineral trappings) during GCS (e.g., Elenius et al., 2012; Zhang et al., 2011; Gasda et al., 2012; Martinez and Hesse, 2016). Each code may have its own limitations and advantages. For instance, CODEBRIGHT is good at solving the mechanics but it currently does not include a sophisticated module for the chemical reaction. TOUGH has an advanced module for chemical reaction but it has to be coupled to other codes when rock deformation is to be modeled (e.g. Kim et al., 2015).

All the above-mentioned codes are written in classical programming languages such as Fortran and C++ and may include graphical user interfaces to ease input and output. The disadvantage of this kind of programming is that the resulting code is rather static and may be limited to some specific types of applications. It is difficult to extend these codes with new features or processes that were not conceived during the initial stage of development. Although this can be improved by object-oriented programming (Rouson et al., 2011), we feel that too often modelling is limited by the capabilities of a particular code. An alternative to the use of classical programming languages is Matlab, a general numerical computing language. The advantage of using Matlab is that it is easy to add new features and processes. Moreover, it can make use of various toolboxes. One of them is MRST (Matlab Reservoir Simulation Toolbox), a finite-volume based method, which has been successfully employed to simulate various subsurface multiphase flow processes, such as heat transport, oil recovery and NAPL removal (e.g. Lie et al., 2012; Lie, 2019; Parvin et al., 2020; Wang et al., 2022).

The objective of this paper is to present a reactive multi-component three-phase flow code for geological carbon sequestration that uses Matlab-based MRST. The structure of the paper represents the necessary stages in code development. First, the conceptual model for general reactive multi-component three-phase flow and corresponding mathematical equations are given in Section 2. The numerical solution of these equations is described in Section 3. Section 4 illustrates this model by means of a specific reactive transport system. The implementation of the numerical method into MRST is presented in Section 5. Section 6 gives benchmark tests of the numerical code and performs sensitive analyses. Section 7 presents a simple application of this code. Finally, Section 8 gives some conclusions.

2. General Reactive Multi-Component Three-Phase Flow Conceptual Model

Reactive multi-component three-phase flow requires the formulation of various partial differential equations that represent mass balances of chemical species or components together with other mathematical equations for quantifying chemical reactions, mass fluxes, phase properties and other constitutive laws. For a better comprehension, we first focus on chemical reactions by formulating mass balances without transport processes. Then we add terms for transport processes.

2.1. Chemical Reaction Module

2.1.1. Chemical System

To simulate a geochemical system where many reactions are taking place in a coupled manner, the first step is to separate the reactions into equilibrium and kinetic reactions (Lasaga, 2014; Langmuir, 1996; Chadwick et al., 2008). If the half time of a reaction is much smaller than the interested time scale, the reaction can be treated as equilibrium. If the half time of a reaction is close to the interested time scale, it should be treated as kinetic. We can neglect the reaction if its time scale is much larger than the interested time scale. This partial equilibrium system, which involves both equilibrium and kinetic reactions, is constrained by the kinetic reaction rate. We note that treating fast reaction as kinetic may require small time steps, which is time-consuming and unnecessary. Thus, it is necessary to assume that fast reactions are at equilibrium, while slow reactions evolve kinetically (Helgeson, 1968; Helgeson et al., 1969; Lichtner, 1985; Steefel and Lasaga, 1994). Kinetic reactions follow rate laws while equilibrium reactions are controlled by the mass action law.

If the reaction system is comprised of n_s species involved in both n_K kinetic and n_E equilibrium reactions, the reaction system can be written as (Leal et al., 2013)

$$\mathbf{0} \rightleftharpoons \boldsymbol{\nu}\boldsymbol{\beta} \tag{1}$$

with

$$\boldsymbol{\nu} = \begin{bmatrix} \boldsymbol{\nu}_k \\ \boldsymbol{\nu}_e \end{bmatrix}, \tag{2}$$

and

$$\boldsymbol{r} = \begin{bmatrix} \boldsymbol{r}_k \\ \boldsymbol{r}_e \end{bmatrix}. \tag{3}$$

Here, the $((n_K + n_E) \times n_s)$-dimensional matrix $\boldsymbol{\nu}$ and the n_s-dimensional vector $\boldsymbol{\beta}$ represent the stoichiometric coefficients and the species, respectively; the $(n_K \times n_s)$-dimensional $\boldsymbol{\nu}_k$ [-] and $(n_E \times n_s)$-dimensional $\boldsymbol{\nu}_e$ [-] are the stoichiometric matrices for kinetic and equilibrium reactions, respectively; and $\boldsymbol{r}_k$ [mol$\cdot$ s^{-1}] and $\boldsymbol{r}_e$ [mol$\cdot$ s^{-1}] denote the kinetic and equilibrium reaction rates, respectively. Furthermore, the chemical species ($\boldsymbol{\beta}$) is comprised of independent kinetic species ($\boldsymbol{\beta}_k$) and other species. Independent kinetic species are only involved in kinetic reactions, while other species can be involved in both kinetic and equilibrium reactions. An example of independent kinetic species is given in Section 4.1.

Kinetic and equilibrium reactions are controlled by different mechanisms. Kinetic reactions are governed by an empirical expression for the reaction rate, while equilibrium reactions are governed by the Mass Action Law (MAL). We can understand the partial equilibrium system as kinetic reaction evolving slowly, which perturbs the equilibrium reactions away from their equilibrium state, followed by an instantaneous adjustment to a new equilibrium state. As a new temporal equilibrium state is reached, the kinetic reaction rate may be changed also. For a closed partial equilibrium system (i.e., without advection or dispersion), the kinetic reaction rates decrease with time, and finally all the (equilibrium and kinetic) species reach equilibrium.

2.1.2. Governing Chemical Reaction Equations

First, each kinetic reaction corresponds to one independent kinetic species that evolves according to a kinetic rate law. Therefore, for n_K kinetic reactions, we can formulate n_K mass balance of n_K independent kinetic species. If no transport is considered, this is expressed by

$$\frac{d\boldsymbol{\xi}_k^*}{dt} = \boldsymbol{M}_{mk}\boldsymbol{\nu}_{kk}^t\boldsymbol{r}_k, \tag{4}$$

where the vector $\boldsymbol{\xi}_k^*$ [kg] and diagonal matrix $\boldsymbol{M}_{mk}$ [kg·mol^{-1}] store the masses and molar masses of the n_K independent kinetic species, respectively, and $\boldsymbol{\nu}_{kk}$ is obtained by extracting the columns corresponding to independent kinetic species from $\boldsymbol{\nu}_k$. Diagonal matrix $\boldsymbol{M}_{mk}$ is used to transfer the unit of chemical reaction rate from [mol·s^{-1}] to [kg·s^{-1}]. The independent kinetic species are not involved in equilibrium reactions. Here, $\boldsymbol{\xi}_k^*$ is used to distinguish it from $\boldsymbol{\xi}_k$ in equation (10), which includes transport processes. The calculation of $\boldsymbol{r}_k$ is given in Appendix B.

Second, all the species should satisfy the n_E equilibrium constraints, given by the mass action law, i.e.,

$$\boldsymbol{\nu}_e \ln \boldsymbol{a} = \ln \boldsymbol{K}_e, \tag{5}$$

where $\boldsymbol{a}$ stores activities of all species and $\boldsymbol{K}_e$ stores the equilibrium constants for n_E equilibrium reactions.

Finally, to solve the masses of the n_s species, we still need $(n_s - n_K - n_E)$ more constraints, which are based on mass balances of components. Components are linear combinations of species and are independent of all reactions. Thus, the mass balances of components in a system without transport are given by

$$\boldsymbol{U}\boldsymbol{\xi} = \boldsymbol{u}_C = \boldsymbol{U}\boldsymbol{\xi}_0, \tag{6}$$

where $\boldsymbol{\xi}$ [kg] and $\boldsymbol{\xi}_0$ [kg], respectively, store the temporal and initial mass of all species, $\boldsymbol{u}_C$ stores the mass of $(n_s - n_K - n_E)$ components, and $\boldsymbol{U}$ is the $(n_s - n_K - n_E)\times n_s$-dimensional kernel matrix only dependent on the stoichiometric

matrix $\boldsymbol{\nu}$. The calculation of $\boldsymbol{U}$ is given in Appendix A.

2.2. Transport Equations

Before formulating the final governing equations for the mass balances of the components, we first give the mass balance of the β-species in α-fluid-phase and solid phase (Saaltink et al., 2013; Carrera et al., 2022):

$$0 = f_\alpha^\beta = \frac{\partial(\phi_\alpha \rho_\alpha X_\alpha^\beta)}{\partial t} + \nabla \cdot (\rho_\alpha X_\alpha^\beta \boldsymbol{q}_\alpha) - \nabla \cdot (\phi_\alpha \boldsymbol{D}_\alpha \rho_\alpha \nabla X_\alpha^\beta) - \boldsymbol{M}_m(\beta,\beta)\boldsymbol{\nu}(:,\beta)^t \boldsymbol{r}' - Q^\beta, \quad \alpha = l, g, s; \tag{7}$$

where, subscripts $\alpha = l, g, s$ denote liquid, gas and solid phases, respectively; $\phi_l = \phi S_l$ and $\phi_g = \phi S_g$ [-] are the volumetric fractions of liquid and gaseous phases, respectively, with ϕ [-] and S [-] representing the porosity and saturation, respectively; $\phi_s = 1 - \phi$ [-] is the volumetric fraction of solid phase; ρ [kg$\cdot$ m^{-3}] represents the density; X_α^β [-] represents the mass fraction of species β in phase α; t [s] is time; $\boldsymbol{q}$ [m$\cdot$ s^{-1}] is the Darcy discharge; $\boldsymbol{D}$ [m$^2\cdot$ s^{-1}] is the dispersion tensor; $\boldsymbol{M}_m$ [kg$\cdot$mol^{-1}] is the diagonal matrix with the (β,β) entry storing the molar mass of the $\beta-$species; $\boldsymbol{\nu}(:,\beta)^t$ denotes the transpose of β-th column vector of stoichiometic matrix $\boldsymbol{\nu}$; $\boldsymbol{r}'(=\boldsymbol{r}/V_0)$[mol$\cdot$m$^{-3}\cdot$s^{-1}] is the reaction rate per unit volume, with V_0 [m^3] being the reference volume; and Q^β [kg$\cdot$ m$^{-3}\cdot$ s^{-1}] is the external source term. For the solid phase, $\boldsymbol{q}_s = \boldsymbol{D}_s = 0$.

Equation (7) consists of a system of n_s equations, each containing a source term due to (kinetic or equilibrium) chemical reaction. Obviously, solving this system of governing equations is computationally expensive, because of the large number of equations and variables, that include the equilibrium reaction rates. Instead of studying the n_s advection dispersion reaction equations (ADREs) for n_s species, we can simplify our problem to $(n_s - n_E - n_K)$ advection diffusion equations (ADEs) for $(n_s - n_E - n_K)$ components that are independent of reaction rates. The governing equations for the mass balances of components are obtained by multiplying each term in equation (7) with kernel matrix $\boldsymbol{U}$, i.e.,

$$0 = f_C = \sum_{\alpha=l,g,s} [\frac{\partial(\phi_\alpha \rho_\alpha X_\alpha^C)}{\partial t} + \nabla \cdot (\rho_\alpha X_\alpha^C \boldsymbol{q}_\alpha) - \nabla \cdot (\phi_\alpha \boldsymbol{D}_\alpha \rho_\alpha \nabla X_\alpha^C)] - \sum_{\beta=1}^{n_s} (U_{C,\beta} Q^\beta), \tag{8}$$

where, the mass fraction of the component is defined as

$$X_\alpha^C = \sum_{\beta \in \alpha} U_{C,\beta} X_\alpha^\beta. \tag{9}$$

In addition, we need n_K transport equations for the n_K independent kinetic species, which are necessary to close

the chemical reaction system as shown in Section 2.1.

$$0 = f_\alpha^{\beta_k} = \frac{\partial(\phi_\alpha \rho_\alpha X_\alpha^{\beta_k})}{\partial t} + \nabla \cdot (\rho_\alpha X_\alpha^{\beta_k} \boldsymbol{q}_\alpha) - \nabla \cdot (\phi_\alpha \boldsymbol{D}_\alpha \rho_\alpha \nabla X_\alpha^{\beta_k}) - \boldsymbol{M}_{mk}(\beta_k, \beta_k) \boldsymbol{\nu}_{kk}(:, \beta_k)^t \boldsymbol{r}'_k - Q^{\beta_k}, \quad \alpha = l, g, s; \tag{10}$$

where, β_k denotes the independent kinetic species; $\boldsymbol{r}'_k (= \boldsymbol{r}_k / V_0)$[mol·m^{-3}·s^{-1}] is the reaction rate per unit volume, with V_0 [m^3] being the reference volume. Note that the transport equation (8) for the component does not contain a source term for any chemical reactions, because multiplication of kernel matrix $\boldsymbol{U}$ with equation (7) eliminates both kinetic and equilibrium reactions (see Appendix A). However, a source term due to kinetic reactions exists in the transport equation (10) for kinetic species.

2.3. Constitutive Equations

To close the transport system we need constitution equations to quantify several properties of the phases and of the porous medium. The constitution equations for the density and viscosity are given in Vilarrasa et al. (2010b). The saturation and the relative permeability are calculated with the model given in Appendix C. For the mobile phases (liquid and gas), the flow rate ($\boldsymbol{q}_\alpha$, $\alpha = l, g$) is given by the extended Darcy's law

$$\boldsymbol{q}_\alpha = -\frac{\kappa_{r\alpha}}{\mu_\alpha} \kappa (\nabla p_\alpha - \rho_\alpha g \nabla z), \tag{11}$$

where, κ_r [-] is the relative permeability; μ [pa · s] is the viscosity; κ [m^2] is the intrinsic permeability; p [pa] is the pressure; z [m] is the depth; and g [m· s^{-2}] is the gravitational acceleration. The intrinsic permeability κ changes with porosity according to Közeny-Carman model (Kozeny, 1927; Carman, 1997; Hommel et al., 2018). The traditional Közeny-Carman model is

$$\kappa = \kappa_0 \left(\frac{\phi}{\phi_0} \right)^{\gamma_c} \left(\frac{1 - \phi_0}{1 - \phi} \right)^2, \tag{12}$$

where, κ_0 is the initial intrinsic permeability and ϕ_0 is the initial porosity. Normally, γ_c is 3.0. The dispersion tensor is given by

$$\boldsymbol{D}_\alpha = \left(D_m + \alpha_T |\boldsymbol{v}_\alpha| \right) \boldsymbol{I} + (\alpha_L - \alpha_T) \frac{\boldsymbol{v}_\alpha \boldsymbol{v}_\alpha^t}{|\boldsymbol{v}_\alpha|}, \tag{13}$$

where $\boldsymbol{I}$ is the identity matrix, D_m [m^2·s^{-1}] is the molecular diffusion coefficient, α_L [m] and α_T [m] are respectively

the longitudinal and transverse dispersivities, and $\boldsymbol{v}_\alpha = \boldsymbol{q}_\alpha/(\phi S_\alpha)$ (Chen et al., 2006; Saaltink et al., 2013).

3. Numerical Solution

We have to solve $n_s - n_E$ partial differential equations that represent the transport of $n_s - n_E - n_K$ components plus n_K kinetic species. We can write these equations as functions of variables that we name independent variables. Several options can be used for the choice of independent variables. In this work, we choose liquid pressure ($\boldsymbol{p}_l$), gas pressure ($\boldsymbol{p}_g$), porosity ($\boldsymbol{\phi}$) and masses of kinetic species ($\boldsymbol{\xi}_k$) and components ($\boldsymbol{u}_C$) as independent variables. Moreover, we distinguish between the main components of each of the three phases (liquid, gas and solid) and the other components. In our specific reactive three-phase flow case (see Section 4), the main liquid component is water (indicated with subscript w), the main gas component is CO_2 (indicated with subscript c) and the main solid component is calcium (indicated with subscript m). The liquid pressure, gas pressure and porosity are associated to the transport equations of the main components of three phases are called independent transport variables. In fact, these main components are similar, though not identical, to the mass balances of the three phases. The other independent variables, i.e., $\boldsymbol{\xi}_k$ and $\boldsymbol{u}_C$, we call independent reaction variables. Hence, we have two groups of independent variables

$$\boldsymbol{x} = \begin{bmatrix} \boldsymbol{p}_l \\ \boldsymbol{p}_g \\ \boldsymbol{\phi} \end{bmatrix} \tag{14}$$

and

$$\boldsymbol{y} = \left[\boldsymbol{\xi}_k, \boldsymbol{u}_C\right]^t. \tag{15}$$

Here, $\boldsymbol{x}$ and $\boldsymbol{y}$, respectively, store the independent transport and reaction variables for all the field grids.

As the independent reaction variables generally have not a large effect on the independent transport variables, the reactive transport system is solved in three steps. First, the three independent transport variables $\boldsymbol{p}_l, \boldsymbol{p}_g, \boldsymbol{\phi}$ are solved based on three selected governing transport equations. Second, the independent reaction variables stored in $\boldsymbol{y}$ are then updated based on the flow field updated with those three independent transport variables. Finally, the chemical reaction are solved cell by cell using the updated independent reaction variables. We first explain the calculation of the independent transport variables stored in $\boldsymbol{x}$ in Section 3.1, then show that of the independent reaction variables stored in $\boldsymbol{y}$ in Section 3.2, and finally describe the solution of the chemical reactions for mass compositions of all species from the obtained independent reaction variables in Section 3.3.

3.1. Solution of Independent Transport Variables

The independent transport variables stored in $\boldsymbol{x}$ (c.f. expression (14)) are solved from three mass balance equations using Newton-Raphson method for water (w), CO_2 (c) and mineral (m) components; that is,

$$0 = f_t^{\mathcal{C}} = \sum_{\alpha=l,g,s} \left[\frac{\partial(\phi_\alpha \rho_\alpha X_\alpha^{\mathcal{C}})}{\partial t} + \nabla \cdot (\rho_\alpha X_\alpha^{\mathcal{C}} \boldsymbol{q}_\alpha) - \nabla \cdot (\phi_\alpha \boldsymbol{D}_\alpha \rho_\alpha \nabla X_\alpha^{\mathcal{C}}) \right] - \sum_{\beta=1}^{n_s} (U_{\mathcal{C},\beta} Q^\beta), \tag{16}$$

where $\mathcal{C} = (w, c, m)$. An example definition of these components is given in Section 4.1.

The Newton-Raphson form of equation (16) is given as

$$\boldsymbol{f}_t(\boldsymbol{x}) = \boldsymbol{0} \tag{17}$$

with

$$\boldsymbol{x} = \begin{bmatrix} \boldsymbol{p}_l \\ \boldsymbol{p}_g \\ \boldsymbol{\phi} \end{bmatrix}; \boldsymbol{f}_t = \begin{bmatrix} \boldsymbol{f}_t^w \\ \boldsymbol{f}_t^c \\ \boldsymbol{f}_t^m \end{bmatrix}. \tag{18}$$

Here, $\boldsymbol{f}_t^w$, $\boldsymbol{f}_t^c$ and $\boldsymbol{f}_t^m$, respectively, store the f_t^w, f_t^c and f_t^m (c.f. equation (16)) for all the field grids.

The Newton-Raphson solution of $\boldsymbol{x}$ based on equation (17) is given as

$$\boldsymbol{J}_t^{i+1,j} [\delta \boldsymbol{x}]^{i+1,j} = -\boldsymbol{f}_t^{i+1,j}, \tag{19}$$

where the Jacobian matrix

$$\boldsymbol{J}_t^{i+1,j} = \left[\frac{\partial \boldsymbol{f}_t}{\partial \boldsymbol{x}} \right]^{i+1,j} = \begin{bmatrix} \frac{\partial \boldsymbol{f}_w}{\partial \boldsymbol{p}_l} & \frac{\partial \boldsymbol{f}_w}{\partial \boldsymbol{p}_g} & \frac{\partial \boldsymbol{f}_w}{\partial \boldsymbol{\phi}} \\ \frac{\partial \boldsymbol{f}_c}{\partial \boldsymbol{p}_l} & \frac{\partial \boldsymbol{f}_c}{\partial \boldsymbol{p}_g} & \frac{\partial \boldsymbol{f}_c}{\partial \boldsymbol{\phi}} \\ \frac{\partial \boldsymbol{f}_m}{\partial \boldsymbol{p}_l} & \frac{\partial \boldsymbol{f}_m}{\partial \boldsymbol{p}_g} & \frac{\partial \boldsymbol{f}_m}{\partial \boldsymbol{\phi}} \end{bmatrix}^{i+1,j}, \tag{20}$$

where, superscripts i and j denote the time step and the iteration number, respectively. The $[\boldsymbol{x}]^{i+1,j}$ is updated according to

$$[\boldsymbol{x}]^{i+1,j+1} = [\boldsymbol{x}]^{i+1,j} + [\delta \boldsymbol{x}]^{i+1,j}, \tag{21}$$

where $[\delta \boldsymbol{x}]^{i+1,j}$ is obtained by solving

$$\boldsymbol{J}_t^{i+1,j}[\delta \boldsymbol{x}]^{i+1,j} = -\boldsymbol{f}_t^{i+1,j}. \tag{22}$$

3.2. Solution of Independent Reaction Variables

In the previous section the independent reaction variables are not calculated, in order to reduce the size of the Jacobian matrix. The independent reaction variables are calculated after solving the independent transport variables. Once having solved the independent transport variables, we can obtain the flow field, such as the porosity, liquid saturation, discharge rate, and so on. In virtue of the flow field, the independent reaction variables ($\boldsymbol{y}$) are solved by explicitly solving equations (8) and (10).

Equation (8) is solved as

$$[u_C]^{i+1,j+1} = [u_C]^i - \Delta t^{i+1} \sum_{\alpha=l,g,s}[\nabla \cdot (\rho_\alpha X_\alpha^C \boldsymbol{q}_\alpha) - \nabla \cdot (\phi_\alpha \boldsymbol{D}_\alpha \rho_\alpha \nabla X_\alpha^C)]^{i+1,j} + \Delta t^{i+1} \sum_{\beta=1}^{n_s}[U_{C,\beta} Q^\beta]^{i+1,j}. \tag{23}$$

Unlike equation (8), which has no chemical reaction term, equation (10) is solved with operator splitting. Firstly, we only consider the mass transport in the governing equation; that is,

$$[\xi_k^*]^{i+1,j+1} = [\xi_k^*]^i - \Delta t^{i+1} \sum_{\alpha=l,g,s}[\nabla \cdot (\rho_\alpha X_\alpha^{\beta_k^*,i} \boldsymbol{q}_\alpha) - \nabla \cdot (\phi_\alpha \boldsymbol{D}_\alpha \rho_\alpha \nabla X_\alpha^{\beta_k^*,i})]^{i+1,j} + \Delta t^{i+1}[Q^{\beta_k^*}]^{i+1,j}. \tag{24}$$

Secondly, the source term due to kinetic reaction will be calculated in the chemical reaction step explained in the next section; that is

$$[\xi_k]^{i+1,j+1} = [\xi_k^*]^{i+1,j+1} + \Delta\xi_{che}^{i+1,j+1}, \tag{25}$$

where, $\Delta\xi_{che}^{i+1,j+1}$ is the mass change due to chemical reaction, which is obtained when implicitly solving equation (26).

The operator splitting moves mass change of the kinetic species due to kinetic reaction from the transport equation to the chemical reaction step. Thus, the kinetic reaction will be calculated simultaneously with the equilibrium reaction in the chemical reaction step. This is different from literature (e.g., Saaltink et al., 1998), where kinetic reactions are solved in the transport equations separated from the equilibrium reactions.

3.3. Solution of Chemical Reactions

Given the independent reaction variables of the previous section, we calculate the masses of all species ($\boldsymbol{\xi}$) by solving equations for the mass balances of kinetic species, definition of components and mass action laws (equations 4) to (6)) simultaneously

$$\begin{bmatrix} \frac{d\xi_k^*}{dt} \\ \boldsymbol{U}\boldsymbol{\xi} \\ \boldsymbol{\nu}_e \ln \boldsymbol{a} \end{bmatrix} = \begin{bmatrix} \boldsymbol{M}_{mk} \boldsymbol{\nu}_{kk}^t \boldsymbol{r}_k \\ \boldsymbol{u}_C \\ \ln \boldsymbol{K}_e \end{bmatrix}. \tag{26}$$

Equations (26) are solved by using the Newton-Raphson method. The Newton-Raphson form of the governing equations is

$$\boldsymbol{0} = \boldsymbol{f}_r = \begin{bmatrix} \frac{d\xi_k^*}{dt} \\ \boldsymbol{U}\boldsymbol{\xi} \\ \boldsymbol{\nu}_e \ln \boldsymbol{a} \end{bmatrix} - \begin{bmatrix} \boldsymbol{M}_{mk} \boldsymbol{\nu}_{kk}^t \boldsymbol{r}_k \\ \boldsymbol{u}_C \\ \ln \boldsymbol{K}_e \end{bmatrix}. \tag{27}$$

The Jacobian matrix of this system of equation is

$$\boldsymbol{J}_r = \frac{\partial \boldsymbol{f}_r}{\partial \boldsymbol{\xi}} = \begin{bmatrix} \frac{1}{dt} \frac{\partial \xi_k^*}{\partial \xi} - \boldsymbol{M}_{mk} \boldsymbol{\nu}_{kk}^t \frac{\partial \boldsymbol{r}_k}{\partial \xi} \\ \boldsymbol{U} \\ \boldsymbol{\nu}_e \frac{\partial \ln \boldsymbol{a}}{\partial \xi} \end{bmatrix}. \tag{28}$$

The solution of equation (26) is

$$\boldsymbol{\xi}^{i+1,j+1} = \boldsymbol{\xi}^{i+1,j} + \delta\boldsymbol{\xi}^{i+1,j}, \tag{29}$$

where $\delta\boldsymbol{\xi}^{i+1,j}$ is obtained by solving a set of linear equations

$$\boldsymbol{J}_r^{i+1,j} \delta\boldsymbol{\xi}^{i+1,j} = -\boldsymbol{f}_r^{i+1,j}. \tag{30}$$

Besides equation (26), the mass of chemical species should also satisfy inequality constraints to ensure that the non-negative mass of any species; that is, $\boldsymbol{\xi} \geq \boldsymbol{0}$. There are two ways to cope with these unwelcome negative values. One method sets the mass in the $(j+1)$th iteration to zero if we obtain a negative value in the $(j+1)$th iteration (Carrera et al., 2004), and the other multiplies the value in the jth iteration by a factor of η_s ($\eta_s < 1$) if we get negative values for the $(j+1)$th iteration (Leal et al., 2013).

Finally, a convergence criterion has to be defined. We base convergence on the relative change of the species, given

as

$$\max \left| \frac{\delta_{\xi}^{i+1,j}}{\xi^{i+1,j+1} + 1} \right| < \epsilon_{\xi}, \tag{31}$$

where ϵ_{ξ} is the tolerance value for the convergence (Leal et al., 2013).

4. Specific Reactive Three-Phase Flow Model for GCS System

4.1. Chemical System

In this section we apply the previous method to GCS with three phases, i.e., two fluid phases (gas and liquid) and one solid phase. We assume the gas phase to consist only of $CO_2(g)$, whereas the liquid phase contains multiple aqueous species. The solid phase only contains calcite. The heterogeneous reaction between calcite and brine is considered kinetic, while the other reactions are treated as equilibrium reactions (Steefel and Van Cappellen, 1990; Steefel and Lasaga, 1994). The chemical system is given as

$$\begin{aligned}
&K1: \ CaCO_3(s) + H^+ = Ca^{2+} + HCO_3^-;\\
&E1: \ CO_2(aq) = CO_2(g);\\
&E2: \ H^+ + HCO_3^- = H_2O + CO_2(aq);\\
&E3: \ HCO_3^- = H^+ + CO_3^{2-};\\
&E4: \ H_2O = H^+ + OH^-.
\end{aligned} \tag{32}$$

In this case, we consider 9 reactive species: H_2O, $CO_2(g)$, $CaCO_3(s)$, H^+, Ca^{2+}, HCO_3^-, $CO_2(aq)$, CO_3^{2-} and OH^-. We also add Na^+ and Cl^- to adjust the salinity of the brine. This is necessary because the salinity of brine can significantly affect the dissolution of CO_2 by changing the ionic strength, as well as change the brine viscosity and density. Here, we assume that Na^+ and Cl^- are not involved in chemical reactions and their molalities are constant, so that transport equations for these species are not necessary. The heterogeneous reaction involving solid calcite ($K1$ of equation (32)) is considered kinetic, because the time scale of the reactions could be similar to that of transport. The time scales of the other reactions are negligible, so that we can assume equilibrium, which decreases the computational burden (Helgeson, 1968; Helgeson et al., 1969; Langmuir, 1996; Lasaga, 2014; Leal, 2014). This assumption has been widely used in geological chemical systems (Saaltink et al., 1998, 2001). We note that the geological system (32) could be modified according to the field data on the fluid and rock compositions (Forster et al., 2006). For instance, we can add the dissolution/precipitation of magnesite and dolomite to (32), if the field data show the rock-forming mineral contains high mass fractions of these minerals.

The stoichiometric matrices for the kinetic reaction and equilibrium reactions in the partial equilibrium chemical system (32) are, respectively,

$$\boldsymbol{\nu}_k = \begin{array}{c} \\ K1 \end{array} \begin{array}{c} \begin{array}{ccccccccc} H_2O & CO_2(g) & CaCO_3(s) & H^+ & Ca^{2+} & HCO_3^- & CO_2(aq) & CO_3^{2-} & OH^- \end{array} \\ \begin{array}{ccccccccc} 0 & 0 & -1 & -1 & 1 & 1 & 0 & 0 & 0 \end{array} \end{array} \tag{33}$$

and

$$\boldsymbol{\nu}_e = \begin{array}{c} \\ E1 \\ E2 \\ E3 \\ E4 \end{array} \begin{array}{c} \begin{array}{ccccccccc} H_2O & CO_2(g) & CaCO_3(s) & H^+ & Ca^{2+} & HCO_3^- & CO_2(aq) & CO_3^{2-} & OH^- \end{array} \\ \begin{array}{ccccccccc} 0 & 1 & 0 & 0 & 0 & 0 & -1 & 0 & 0 \\ 1 & 0 & 0 & -1 & 0 & -1 & 1 & 0 & 0 \\ 0 & 0 & 0 & 1 & 0 & -1 & 0 & 1 & 0 \\ -1 & 0 & 0 & 1 & 0 & 0 & 0 & 0 & 1 \end{array} \end{array} . \tag{34}$$

As explained in Appendix A, the kernel matrix ($\boldsymbol{U}$) for the mass components is calculated as

$$\boldsymbol{U} = \begin{array}{c} \\ w \\ c \\ m \\ \mathrm{pH} \end{array} \begin{array}{c} \begin{array}{ccccccccc} H_2O & CO_2(g) & CaCO_3(s) & H^+ & Ca^{2+} & HCO_3^- & CO_2(aq) & CO_3^{2-} & OH^- \end{array} \\ \begin{array}{ccccccccc} 1 & 0 & 0 & 0 & -0.44950 & 0.29525 & 0 & 0.30020 & 1.05921 \\ 0 & 1 & 0 & 0 & -1.09811 & 0.7212 & 1 & 0.73339 & 0 \\ 0 & 0 & 1 & 0 & 2.49730 & 0 & 0 & 0 & 0 \\ 0 & 0 & 0 & 1 & 0.05029 & -0.01652 & 0 & -0.03359 & -0.05925 \end{array} \end{array} . \tag{35}$$

We can see that the number of species n_s=9, the number of kinetic reaction $n_K = 1$, the number of equilibrium reactions n_E=4, and the number of components $n_s - n_K - n_E$=4. We need n_K=1 more constraints based on the independent kinetic species. Both $CaCO_3(s)$ and Ca^{2+} can be selected as the independent kinetic species. Here we select calcite. Then the independent reaction variables, which are used to solve the chemical reactions, are

$$\boldsymbol{y} = \left[\boldsymbol{\xi}_k, \boldsymbol{u}_C\right]^t = \left[\boldsymbol{\xi}_{calcite}, \boldsymbol{u}_w, \boldsymbol{u}_c, \boldsymbol{u}_m, \boldsymbol{u}_{\mathrm{pH}}\right]^t . \tag{36}$$

The kinetic reaction requires a rate law, for which we use an empirical model explained in Appendix B.

4.2. Transport Equations

The first three rows of the kernel matrix ($\boldsymbol{U}$) of equation (35) refer to the main components. The transport equations of these components are used to solve the three independent transport variables stored in $\boldsymbol{x}$. The transport equations

are based on equation (16) and in this specific case becomes

$$0 = f_w = \frac{\partial(\phi S_l \rho_l X_l^w)}{\partial t} + \nabla \cdot (X_l^w \rho_l \boldsymbol{q}_l) - \nabla \cdot (\phi S_l \rho_l \boldsymbol{D}_l \nabla X_l^w) - \sum_{\beta=1}^{9} [U_{w,\beta} Q^\beta], \tag{37}$$

$$0 = f_c = \frac{\partial(\phi S_l \rho_l X_l^c)}{\partial t} + \frac{\partial(\phi S_g \rho_g)}{\partial t} + \nabla \cdot (X_l^c \rho_l \boldsymbol{q}_l) + \nabla \cdot (\rho_g \boldsymbol{q}_g) - \nabla \cdot (\phi S_l \rho_l \boldsymbol{D}_l \nabla X_l^g) - \sum_{\beta=1}^{9} [U_{c,\beta} Q^\beta], \tag{38}$$

$$0 = f_m = \frac{\partial(\phi S_l \rho_m X_l^m)}{\partial t} + \frac{\partial((1-\phi)\rho_m)}{\partial t} + \nabla \cdot (X_l^m \rho_l \boldsymbol{q}_l) - \nabla \cdot (\phi S_l \rho_l \boldsymbol{D}_l \nabla X_l^m) - \sum_{\beta=1}^{9} [U_{m,\beta} Q^\beta]. \tag{39}$$

Here, we have assumed that the gas phase only contains $CO_2(g)$, the solid phase only contains calcite, and we only inject pure $CO_2(g)$. The independent transport variables are solved based on equations (37) to (39) using the Newton-Raphson method given in Section 3.1.

The transport equation for the kinetic species and all components can be used to calculate the independent reaction variables stored in $\boldsymbol{y}$ (c.f. expression (36)). According to equation (23), the values of these independent reaction variables are explicitly updated as

$$[\xi^*_{calcite}]^{i+1,j+1} = [\xi^*_{calcite}]^i \tag{40}$$

$$[u_w]^{i+1,j+1} = [u_w]^i - \Delta t^{i+1} [\nabla \cdot (\rho_l X_l^w \boldsymbol{q}_l) - \nabla \cdot (\phi_l \boldsymbol{D}_l \rho_l \nabla X_l^w)]^{i+1,j} + \Delta t^{i+1} \sum_{mw=1}^{MW} [U_{w,C} Q^C]^{i+1,j}, \tag{41}$$

$$[u_c]^{i+1,j+1} = [u_c]^i - \Delta t^{i+1} [\nabla \cdot (\rho_l X_l^c \boldsymbol{q}_l) + \nabla \cdot (\rho_g \boldsymbol{q}_g) - \nabla \cdot (\phi_l \boldsymbol{D}_l \rho_l \nabla X_l^c)]^{i+1,j} + \Delta t^{i+1} \sum_{mw=1}^{MW} [U_{c,C} Q_l^C]^{i+1,j}, \tag{42}$$

$$[u_m]^{i+1,j+1} = [u_m]^i - \Delta t^{i+1}[\nabla \cdot (\rho_l X_l^m \boldsymbol{q}_l) - \nabla \cdot (\phi_l \boldsymbol{D}_l \rho_l \nabla X_l^m)]^{i+1,j} + \Delta t^{i+1} \sum_{mw=1}^{MW} [U_{m,C} Q^C]^{i+1,j}, \quad (43)$$

$$[u_{\mathrm{pH}}]^{i+1,j+1} = [u_{\mathrm{pH}}]^i - \Delta t^{i+1}[\nabla \cdot (\rho_l X_l^{\mathrm{pH}} \boldsymbol{q}_l) - \nabla \cdot (\phi_l \boldsymbol{D}_l \rho_l \nabla X_l^{\mathrm{pH}})]^{i+1,j} + \Delta t^{i+1} \sum_{mw=1}^{MW} [U_{\mathrm{pH},C} Q^C]^{i+1,j}. \quad (44)$$

5. Code Design

The code is developed based on the Matlab Reservoir Simulation Toolbox (MRST) library, which is specialized for multiphase flow in porous media (Lie, 2019). The architecture of the code is shown in Figure 1. The simulation is performed by running the executive file, which is comprised of two sections, the initialization section and the reactive transport solver, both including five modules. The grid processing module is in charge of the grid topology, which can be either structural or nonstructural (Lie, 2019). The fluid property module is in charge of fluid properties (e.g., relative permeability and retention curve); herein, we employed the Van Genuchten model given in Appendix C. The well module defines the well position and other well parameters such as the well index and the mass composition of the injected fluid. Detailed definition of the well can be found in Wang (2022). The boundary module defines the boundary condition, which can be either closed or open with constant liquid pressure. The reaction module is responsible for chemical reactions for the chemical system given in Section 4.1.

In general the simulation is implemented with seven steps, as shown in Table 1. After Steps 1 to 6, we generate a numerical task that will be solved with the reactive transport solver in Step 7.

6. Benchmark Test and Simple Sensitive Analysis

The developed numerical model is verified against the one-dimensional theoretical solution proposed by McWhorter and Sunada (1990). Besides, a simple sensitivity analysis is done of the kinetic reaction rate parameters.

6.1. Description

The benchmark consists of a one-dimensional domain shown in Figure 2, and the parameter setting for the system is listed in Table 2. The left boundary is closed while the right boundary has constant liquid pressure, and zero gradients of saturation and porosity. An injection well, of which the radius is r_w, is added to the left of the domain, where CO_2 is injected at a rate of $Q_{g,m} = \overline{\rho}_g A/\sqrt{t}$, that is, the injection rate decreases from an initially infinite value to zero; here, $\overline{\rho}_g$ is the mean gas density, and A depends on the maximum expected gas saturation, S_{g0}, which appears at the injection point, i.e., $x = 0$ (McWhorter and Sunada, 1990). The initial time step Δt^0 should be as small as possible to

Table 1
Implementation of the reactive transport model through the modules given in Figure 1.

Step 1.	Domain design: set the length scale of the domain, and discretize the domain. In this step, we generate object `Grid` that stores the topology of the field. In this procedure, the grid processing module is employed.
Step 2.	Rock properties: assign porosity and intrinsic permeability to each grid cell. In this step, we generate object `Rock` that stores the rock property of each grid cell.
Step 3.	Fluid properties: define the relative permeability and retention curves of the fluid phases. In this step, we generate object `Fluid` that contains the functions for the relative permeability and retention curves. The fluid properties is defined through fluid property module.
Step 4.	Injection Wells: we generate object `Well` that contains well information, e.g., injection rate, well index, pierced grids, etc. The well module is in charge of the generation of the injection well.
Step 5.	State variables: we initialize the state variables (e.g., gas/brine pressures, mass fractions, dispersion coefficients, etc.) and store them in object `State`. In this step, the reaction module is needed to initialize the chemical composition.
Step 6.	Boundaries: we define the boundary condition and store them in object `bc`. The boundary is added through the boundary module.
Step 7.	Main loop: based on the information given by the aforementioned steps, we update the state variables stored in the object `State` with reactive transport solver. The reactive transport solver contains the numerical solution given in Section 3.

capture the large initial injection rate.

The relative permeability and retention curves are given by the van Genuchten model, which is scaled by two parameters (α_p, m_p) (c.f. Appendix C). The densities (ρ_l, ρ_g) and viscosities (μ_l, μ_g) are calculated with the empirical models given in Riaño-Vilarrasa (2012). The hydrodynamic dispersion is not included and only the molecular diffusion (D_m) is considered.

We use the geochemical system from Section 4. The calcite dissolution model is given in Appendix B, and the values for the parameters are listed in Table 3 (Palandri and Kharaka, 2004). The dissolution of calcite is controlled by acid, neutral and carbonate kinetic mineral mechanisms, of which the rate constants at 25 °C are, respectively, $(k_{0,1}, k_{0,2}, k_{0,3})$. The activation energies of these three mechanisms are, respectively, (E_1, E_2, E_3). θ_{H^+} is the exponent for acid kinetic mechanism and $\theta_{p_{CO_2}}$ is the exponent for carbonate mechanism. The shape factor for the reactive surface area is η_V. The effective reactive area per volume of mineral is $\mathcal{A}_s$. We use different values of $\mathcal{A}_s$ to adjust the kinetic reaction rate. The infinite value of $\mathcal{A}_s$ means that the dissolution of calcite is treated as equilibrium reaction, while the zero value of $\mathcal{A}_s$ means that the dissolution of calcite is not considered. The reference value of $\mathcal{A}_s$ is $0.0469 \cdot 10^6$ $[\mathrm{m}^{-1}]$ (Vialle et al., 2014). This value generates a very fast reaction rate.

Initially, the liquid and gas pressure are uniform with liquid pressure being higher, which means saturation with brine. The simulation is terminated (at t_s) when the saturation change at the inlet becomes insignificant.

Regarding the benchmark test, our numerical model is not identical to the theoretical model of McWhorter and Sunada (1990). The theoretical model is a simple incompressible two-phase flow model. Slightly different from the theoretical model, the numerical model considers the reactions among the gas, liquid and rock, as well as the compressibilities of the fluids. However, the two models are comparable because the main influencing factors- the

Table 2
Parameter settings for the flow system.

Parameters	Symbol	Units	Values
Section area	A_f	[m^2]	1
Length	L	[m]	10
Grid discretization	N	[-]	500
Initial permeability	κ^0	[m^2]	1×10^{-11}
Initial porosity	ϕ^0	[-]	0.2
Initial liquid pressure	p_l^i	[bar]	150
Initial gas pressure	p_g^i	[bar]	$145^a(10^b)$
Initial brine/gas saturation	$(S_{l,i}, S_{g,i})$	[-]	(1,0)
Salinity	m_l^S	[molal]	0.5
Temperature	T_c	[°C]	60
Molecular diffusion coefficient	D_m	[m^2·s^{-1}]	10^{-9}
Mean brine/gas viscosity	$(\overline{\mu}_l\ ,\overline{\mu}_g)$	[mpa·s]	(1.5,0.045)
Mean brine/gas density	$(\overline{\rho}_l\ ,\overline{\rho}_g)$	[kg·m^{-3}]	(1010,590)
Parameter for Eq. (58)	α_p	[bar^{-1}]	5
Parameter for Eq. (58)	m_p	[-]	0.8
Well radius	r_w	[m]	0.01
Max expected gas saturation	S_{g0}	[-]	0.101
Initial time step	Δt^0	[s]	10^{-6}
Reference injection rate	A	[kg·s^{-1}]	0.1012
Total simulation time	t_s	[s]	9839

[a] 145 bar is used for the benchmark test;
[b] 10 bar is used in the simple sensitivity analysis.

injection rate, the relative permeability and retention curves- are the same. The discrepancies of density and viscosity due to the compressibility is very small. In the benchmark test, we also minimize the effect of gaseous CO_2 on the chemical reaction, by using already quasi CO_2-saturated brine, i.e., the initial gas pressure ($p_g^i = 145$ bar) is close to the liquid pressure ($p_l^i = 150$ bar). Therefore, we can use the theoretical solution as a benchmark for the numerical model. As we will see, the numerical result agrees well with the theoretical one.

Regarding the simple sensitivity analysis, we only analyze the effect of kinetic reaction rate. To get an obvious comparison between different kinetic reaction rates (as will be shown in Figures 4 to 10), we set the initial gas pressure to a small value of 10 bar. In addition to the reference value of $\mathcal{A}_s$ =0.0469·10^6 [m^{-1}], we also use smaller values, 0.0469·10^2 and 0.0469·10^{-2} [m^{-1}], for $\mathcal{A}_s$, to observe a visual effect of the kinetic reaction rate on the injection process. We also use $\mathcal{A}_s = 0$ [m^{-1}] to test if the program will give zero change of the porosity when there is no calcite dissolution.

6.2. Results

Benchmark with Theoretical Model by McWhorter and Sunada (1990)

The comparison of the saturation distribution calculated with the theoretical model by McWhorter and Sunada (1990) and the numerical results is given in Figure 3. In the numerical simulations the initial liquid pressure is 150 bar and the initial gas pressure (or CO_2 pressure) is 145 bar, which means that the brine has initially a high concentration

Table 3
Parameter settings for kinetic reaction.

Parameter	Value
$\mathcal{A}_s$[m^{-1}]	(inf,0.0469 $\cdot 10^6$,0.0469$\cdot 10^2$,0.0469$\cdot 10^{-2}$,0)[a]
$\theta_{H^+}, \theta_{P_{CO_2}}, \eta_V$[-]	1,1,2/3
(E_1, E_2, E_3) [10^3J·mol^{-1}]	(14.4,23.5,35.4)
($k_{0,1}, k_{0,2}, k_{0,3}$) [mol·m^{-2}·s^{-1}]	($10^{-0.3}, 10^{-5.81}, 10^{-3.48}$)

[a] different $\mathcal{A}_s$ are used to adjust the reaction rate.

of dissolved CO_2 which prevents a large amount of subsequent CO_2 dissolution. The numerical results are obtained when the reaction rate is zero and infinite, i.e., $\mathcal{A}_s = 0$ and inf. When the reaction rate is zero, we do not consider the calcite dissolution, while when the reaction rate is infinite, the precipitation/dissolution of calcite is at equilibrium. From Figure 3, we can see that the numerical results agree very well with the theoretical solution. Because of the very low dissolution of CO_2 into brine, the results from the numerical simulations are slightly smaller than the theoretical one, but the discrepancy between the numerical and theoretical results is negligible.

Simple Sensitive Analysis on Reaction Rate

We also analyze the effect of the kinetic reaction rate by changing the specific area, $\mathcal{A}_s$. In the following simulations, the initial gas pressure of the domain is set to 10 [bar], and initially the system is at chemical equilibrium. The reference value of $\mathcal{A}_s = 0.0469 \cdot 10^6$ [m^{-1}] leads to a reaction time scale of around 10^{-3} [s]. This chemical reaction time scale is much smaller than the transport time scale, which means the kinetic reaction is at quasi equilibrium.

The saturation distributions of the gas phase are given in Figure 4, from which we can see that the results for different $\mathcal{A}_s$ are very similar. This means that the dissolution of calcite has little effect on the dissolution of CO_2.

However, as can be seen from Figure 5, different $\mathcal{A}_s$ can lead to significantly different changes of porosity, i.e., different dissolution of calcite. If we compare the porosity changes in Figure 5, we can find that the results for $\mathcal{A}_s = 0.0469 \cdot 10^6$ and $\mathcal{A}_s = 0.0469 \cdot 10^2$ are very similar, and both of them are larger than the result for $\mathcal{A}_s = 0.0469 \cdot 10^{-2}$. This means that the kinetic dissolution of calcite can be treated as equilibrium reaction when $\mathcal{A}_s > 0.0469 \cdot 10^2$. When $\mathcal{A}_s = 0.0469 \cdot 10^{-2}$, the dissolution of calcite is so slow that we can only observe very small change of porosity, and the change of the porosity decreases with the distance to the injection point because the time of exposure to the $CO_2(g)$ decreases with this distance. In Figure 5, we also show that the porosity change is around 10^{-14}, which is practically zero, when $\mathcal{A}_s = 0$. If we compare Figures 5 and 6, we can see that the permeability change is more sensitive than the porosity change.

From Figure 5, We can also see that the porosity change is very small even for the cases with fast reaction rates. This is because only injecting CO_2 does not change much the saturation index of calcite in brine. To further increase the dissolution of the calcite, we need to inject water without Ca^{2+}. This indicates that the porosity change due to gas

injection cannot be explained with the traditional dissolution model, where acidified brine is continuously injected into the initially brine-saturated domain. The traditional model (as illustrated in the following section) will significantly enhance the dissolution because the injected 'fresh' acidified brine does not contain Ca^{2+}.

The results for pH and molality of $CO_2(aq)$ are shown in Figures 7 and 8, from which we can see that the pH is higher for higher kinetic reaction rate (i.e., large $\mathcal{A}_s$), but the molalities of $CO_2(aq)$ are the same for all cases. This is because the dissolution of CO_2 is a fast equilibrium reaction, which instantly decreases the pH, while the generated H^+ reacts with the calcite at different rates.

The gas pressure, as shown in Figure 9, is closely related to the molality of $CO_2(aq)$ given in Figure 8. The capillary pressure, given in Figure 10, is closely related to the saturation distribution given in Figure 4.

The reaction time scales are 10^{-3} and 10^{1} [s] for $\mathcal{A}_s = 0.0469 \cdot 10^6$ and $\mathcal{A}_s = 0.0469 \cdot 10^2$, respectively, and the maximum transport time step is <60 [s]. This means that in large scale simulations with large times step (e.g. 1 hour) calcite dissolution can be safely treated as an equilibrium reaction. Finally, by observing that the gas saturation in the case with high initial gas pressure (c.f. Figure 3) is much larger than that in the case with low initial gas pressure (c.f. Figure 4), we can conclude that dissolution of CO_2 can strongly affect the GCS process.

7. Simple Application to Analysis of Partial Dissolution

Because in GCS the injected $CO_2(g)$ tends to dissolve the calcite of the rock, it may change porosity and permeability, developing highly permeable channels that affect the CO_2 migration process. This section will illustrate the use of our code to qualitatively analyze the effect of dissolution rate and initial permeability heterogeneity on the development of wormholes. In order to be consistent with the traditional study on calcite dissolution (Hao et al., 2013; Smith et al., 2013), we also inject acidified brine rather than CO_2 gas. As such, in this particular case, we only have rock and brine phases.

7.1. Setup Description

The simulation domain is shown in Figure 11. The initial permeability distribution κ_0 is generated with the Sequential Gaussian Simulation method implemented into the SGSIM code (Journel and Huijbregts, 1976). The natural logarithm heterogeneous permeability field Y $(= \ln \kappa_0)$ follows a correlated random space function, characterized by an anisotropic exponential covariance function with variance of σ_Y^2, x-direction integral scale l_x^0, and y-direction integral scale l_y^0. Different variances are employed to test the effect of the permeability distribution on the partial erosion. Here, we use a small domain, because dissolution can be very heterogeneous at small-scales (Hao et al., 2013). The left boundary has constant brine flux. The injected brine does not contain Ca^{2+}. Five pore volumes are injected with mean Darcian flux of 10^{-5} [m·s^{-1}] during the simulation. The right boundary has constant liquid pressure, p_{lb}, which

Table 4
Parameter settings for the flow system.

Parameter	Symbol	Units	Values
Domain size	(L_x, L_y, L_z)	$[10^{-3}\text{m}]$	$(20, 10, 5)$
Grid discretization	(N_x, N_y, N_z)	[-]	(40,20,1)
Initial geometric mean permeability	κ_g^0	$[\text{m}^2]$	1×10^{-11}
Correlation length of permeability	(l_x^0, l_y^0)	$[10^{-3}\text{m}]$	(13.3,5)
Variance of log permeability	$(\sigma_Y^0)^2$	[-]	0.1,1
Initial porosity	ϕ^0	[-]	0.2
Molecular diffusion coefficient	D_m	$[\text{m}^2\cdot\text{s}^{-1}]$	10^{-9}
Mass fraction of $NaCl$	m_l^S	[molal]	0.5
Temperature	T_c	[°C]	60
Initial liquid pressure	p_l^i	[bar]	150
Initial gas pressure	p_g^i	[bar]	1
Gas pressure of injected brine	$p_{g,inj}$	[bar]	145
Injection rate	q_{inj}	$[\text{m}^3\cdot\text{s}^{-1}]$	$5\cdot10^{-10}$
Total simulation time	T_s	[s]	2000

is equal to the initial liquid pressure. The other boundaries are impermeable. Regarding the fluid property, the hydrodynamic dispersion is not included and only the molecular diffusion (D_m) is considered. The chemical characters are the same as those in Section 6. Here, we also adjust the reaction rate by changing $\mathcal{A}_s$. In addition to the reference value of $\mathcal{A}_s$ =0.0469·10^6 [m^{-1}], we use a smaller value of 0.0469·10^{-2} [m^{-1}] for $\mathcal{A}_s$, to analyse the effect of the kinetic reaction rate on the injection process. Details on parameters are listed in the Table 4.

7.2. Results

We first discuss the results of the field with moderate heterogeneity, i.e., $(\sigma_Y^0)^2 = 1$. Figure 13 shows the distributions of the porosity change, the pH, the molality of $CO_2(aq)$ and of Ca^{2+} in the field with $(\sigma_Y^0)^2 = 1$; the left column gives results for the case with slow chemical reaction, while the right column gives results for the case with normal chemical reaction. If we compare the results for the porosity changes, we can see that (1) when the reaction rate is slow, the porosity change is relatively high in the region with higher initial permeability (c.f. Figure 12), and (2) when normal reaction rate is employed, the porosity change concentrates at the entrance. This is because of the high reaction rate. The injected acidified brine instantaneously reacts with the calcite, the injected liquid almost instantaneously equilibrates with calcite, and the generated Ca^{2+} decreases the erosion ability of the injected liquid. If we compare the results for the pH value, we can see that pH value in the case with slow reaction rate is slightly lower, because the dissolution of calcite, which consumes H^+ (c.f. equation (32)), is slower. If we compare the results for the molality of $CO_2(aq)$, we can see negligible difference between the cases with different reaction rates; this means that the dissolution of calcite has negligible effect on the molality of $CO_2(aq)$. If we observe the result for the molality of Ca^{2+} ($m_l^{Ca^{2+}}$) of the case with slow reaction rate, we can see that $m_l^{Ca^{2+}}$ is lower in the invaded region. This is because the injected brine has no Ca^{2+} and the generation rate of Ca^{2+} is small due to the slow reaction rate. If we observe the

result for the molality of Ca^{2+} ($m_l^{Ca^{2+}}$) of the case with normal reaction rate, we can see that $m_l^{Ca^{2+}}$ is higher in the invaded region. This is because the injected brine instantaneously reacts with the calcite and generates a huge amount of Ca^{2+}.

Figure 14 shows the evolution of the porosity distribution for the field with $(\sigma_Y^0)^2 = 1$. From Figure 14, we can see that if the reaction rate is slow, the acidified brine can generate wormholes along the high permeable region (c.f. Figure 12) (Golfier et al., 2002). If the reaction rate is high, the acidified brine preferentially erodes the calcite at the inlet. This indicates that, for a given injection rate, the dissolution pattern is affected by the reaction rate.

Similarly, we show, in Figures 15 and 16, the results for the field with $(\sigma_Y^0)^2 = 0.1$. Figure 15 shows the distributions of porosity change ($(\phi - \phi_0)/\phi_0$), pH, molality of $CO_2(aq)$ ($m_l^{CO_2(aq)}$) and of Ca^{2+} ($m_l^{Ca^{2+}}$). From Figures 13 and 15, we can see that the result for the field with small heterogeneity (i.e., $(\sigma_Y^0)^2 = 0.1$) shows similar distributions of the ($(\phi - \phi_0)/\phi_0$), pH, molality of $CO_2(aq)$ ($m_l^{CO_2(aq)}$) and molality of Ca^{2+} ($m_l^{Ca^{2+}}$), except that the profile is more uniform in the field with $(\sigma_Y^0)^2 = 0.1$. The porosity evolution for the slow and normal reaction rates are shown in Figure 16.

If we compare the results for gas injection given in Figure 5 and those for acidified brine injection given in Figures 14 and 16, we can see that (1) the dissolution penetrates more but the total amount is small in the case of gas injection with normal reaction rate, while (2) the dissolution concentrates at the entrance but the total amount is large in the case of acidified brine injection with normal reaction rate. Thus we can conclude that the traditional two-phase (i.e., rock and brine) model cannot represent the three-phase (i.e., rock, brine and gas) case in GCS.

8. Conclusions

We have developed a numerical code for reactive multi-phase transport system in GCS (Geological Carbon Sequestration). The code considers multiphase flow of brine and gas (composed of supercritical CO_2) and various chemical reactions including dissolution-precipitation of calcite, that can affect porosity and permeability. The numerical solution is done in three steps. First the pressures of brine and gas and the porosity of all cells are solved simultaneously from the transport equations of the main components for brine, gas and solid rock, for which the method of Newton-Raphson is applied. Second, other transport equations are used to calculate concentrations of kinetic species and components in a straightforward way. Third, the chemical system is solved also using the Newton-Raphson method, which can be done cell by cell.

The code is implemented in Matlab and uses the MRST (Matlab Reservoir Simulation Toolbox) for the discretization of the domain by the finite volume method. This permits to obtain a code that is flexible and easily extensible. Other chemical reactions or fluid properties can be easily changed or added by changing the reaction model or fluid property module. Also, the assignation of parameter becomes more flexible, as this is done in the code itself. An

example, presented in this paper, is the calculation of the initial permeability field by using geostatistical methods.

The code is verified by the one-dimensional theoretical solution of McWhorter and Sunada (1990). Moreover, a sensitive analysis of this model shows that (i) the gas dissolution is negligibly affected by rock dissolution, (ii) the fractional porosity increase due to gas injection is only around 10^{-3} at normal reaction rate, and (iii) the calcite dissolution can be treated as equilibrium reaction at reservoir condition.

We also applied the numerical code to the simulation of calcite dissolution in two-dimensional heterogeneous fields. Initially the brine has a low gas pressure (i.e., low $CO_2(aq)$ concentration and high pH). Brine saturated with high gas pressure is injected at the left boundary. Results show that (i) calcite dissolves mainly at the inlet when the reaction rate law is fast, (ii) effects on pH and $CO_2(aq)$ are seen further away from the acidified brine injection even if the dissolution only appears at the inlet when the rate law is fast, and (iii) dissolution develops in the region of high initial permeability when a slow rate law is used. The traditional two-phase (i.e., rock and brine) model, in which acidified brine is injected into the formation, cannot represent the three-phase (i.e., rock, brine and gas) case in GCS, in which gaseous CO_2 is injected into the formation. Under reservoir condition, the two-phase model predicts concentrated dissolution at the inlet, whereas the dissolution penetrates more according to the three-phase flow model.

Acknowledgments This work was partially supported by the European Commission, through project MARSOLUT (grant H2020-MSCA-ITN-2018); by the Spanish Ministry of Economy and Competitiveness, through project MONOPOLIOS (RTI 2018-101990-B-100, MINECO/ FEDER); and by the Catalan Agency for Management of University and Research Grants through FI 2017 (EMC/2199/2017).

426 **Code availability section**

427 Name of the code/library: MRST_CO2

428 Contact:yufei.wang@upc.edu,daniel.fernandez.g@upc.edu,maarten.saaltink@upc.edu

429 Hardware requirements: normal PC

430 Program language: Matlab

431 Software required: Matlab

432 Program size: 4 Mb

433 The source codes are available for downloading at the link: https://zenodo.org/record/6956860

A. Kernel Matrix

The mass components ($\boldsymbol{u}$), independent on chemical reactions, are stored in $(n_s - n_K - n_E)$-dimensional vector defined as

$$\boldsymbol{u}_C = \boldsymbol{U}\boldsymbol{\xi} = \boldsymbol{U}\boldsymbol{\xi}_0, \tag{45}$$

that is

$$\frac{d\boldsymbol{u}_C}{dt} = \boldsymbol{U}\frac{d\boldsymbol{\xi}}{dt} = \boldsymbol{U} \times \boldsymbol{M}_m \times \boldsymbol{\nu}^t \boldsymbol{r} = \boldsymbol{0}. \tag{46}$$

Therefore, the kernel matrix ($\boldsymbol{U}$) should satisfy

$$\boldsymbol{U} \times \boldsymbol{M}_m \times \boldsymbol{\nu}^t = \boldsymbol{0}, \tag{47}$$

with diagonal matrix $\boldsymbol{M}_m$ storing the molar masses of all the species. The method of calculating $\boldsymbol{U}$ is given in the following.

Let $\boldsymbol{\nu}' = \boldsymbol{\nu}\boldsymbol{M}_m^t$, and equation (47) is changed to

$$\boldsymbol{U}\boldsymbol{\nu}'^t = \boldsymbol{0}. \tag{48}$$

The solution to equation (48) is not unique. A convenient way to construct $\boldsymbol{U}$ is (Saaltink et al., 1998, 2013)

$$\boldsymbol{U} = [\boldsymbol{I}| - \boldsymbol{\nu}'^t_1(\boldsymbol{\nu}'^t_2)^{-1}], \tag{49}$$

where, we have split the stoichiometric matrix into $(n_E + n_K) \times (n_s - n_E - n_K)$ $\boldsymbol{\nu}'_1$ and $(n_E + n_K) \times (n_E + n_K)$ $\boldsymbol{\nu}'_2$, i.e., $\boldsymbol{\nu}' = [\boldsymbol{\nu}'_1|\boldsymbol{\nu}'_2]$.

B. Kinetic Reaction Rate

For a given kinetic dissolution/precipitation reaction, the kinetic reaction rate (r_k [mol·s^{-1}]) is given as (Steefel and Lasaga, 1994; Steefel and Mäher, 2009; Palandri and Kharaka, 2004; Lasaga, 2014; Leal, 2014; Tutolo et al., 2015b)

$$r_k(T_k, p_l, p_g, \boldsymbol{\zeta}) = \mathcal{A}(\boldsymbol{\zeta}) \sum_i \mathcal{K}_i(T_k, p_l, p_g, \boldsymbol{\zeta}), \tag{50}$$

where, $\mathcal{A}$ [m^2] is the surface area of the mineral, $\mathcal{K}_i$ [$mol \cdot m^{-2} \cdot s^{-1}$] is the ith kinetic mechanism function, p_l and p_g are, respectively, liquid and gas pressures, and T_k is temperature in Kelvin. Some common kinetic reaction mechanisms are neutral, acid, base and carbonate, etc (Palandri and Kharaka, 2004). For the case of calcite dissolution there are three involved kinetic reaction mechanisms: neutral, acid and carbonate.

The surface area, $\mathcal{A}$, changes as the mineral dissolves or precipitates. The dynamic model for $\mathcal{A}$ is complex even in batch reactions. Parkhurst and Appelo (2013) offer a simple dynamic model for surface area of the minerals:

$$\mathcal{A} = \mathcal{A}_0 (\frac{V}{V_0})^{\eta_V} = \mathcal{A}_s \cdot V_0 \cdot (\frac{V}{V_0})^{\eta_V}, \tag{51}$$

where, $\mathcal{A}_0$ is the initial surface area of the (solid) mineral species, V_0 [m^3] is the initial volume of the mineral species, and $\mathcal{A}_s$ [$m^2 \cdot m^{-3}$] is the effective reactive area per volume of minerals. $\eta_V = 2/3$ for spheres and cubes that uniformly react with liquid phase.

A general empirical rate equation for the ith kinetic mineral mechanism is given as

$$\mathcal{K}_i = \mathrm{sgn}(1 - I_S) \mid 1 - I_S^{\eta_{i,1}} \mid^{\eta_{i,2}} \eta_{i,c} k_i, \tag{52}$$

where, I_S is the saturation index, given as

$$\ln I_S = \sum_i \nu_i \ln a_i - \ln K, \tag{53}$$

where, a_i and ν_i are, respectively, the activity and stoichiometric value of aqueous species involved in the dissolution/precipitation of the mineral (Sjöberg, 1976; Nancollas and Reddy, 1971), and K is the equilibrium constant for the interested mineral dissolution/precipitation. The exponents $\eta_{i,1}$ and $\eta_{i,2}$ are usually lacking in literature. Note, the activity of the solid mineral species is assumed to be unit. Here, we use $\eta_{i,1} = 1$ and $\eta_{i,2} = 1$.

$\eta_{i,c}$ is a function to model the aforementioned kinetic mineral mechanisms, given as

$$\eta_{c,i} = \prod_j a_j^{\theta_j} \prod_k p_k^{\theta_k}, \tag{54}$$

where, p_k is the partial pressure of the k-th gaseous species, the exponents θ_j and θ_k are from experiment. Positive and negative exponents, respectively, indicate catalyst and inhibitor. For example, θ_{H^+} is nonzero for acid kinetic mechanism, $\theta_{p_{CO_2}}$ is nonzero for carbonate mechanism, and all θ_j and θ_k are zeros for neutral mechanism (Leal, 2014).

The reaction rate constant k_i [mol·m^{-2}·s^{-1}] is given as

$$k_i = k_{0,i} \exp\left[-\frac{E_i}{R}\left(\frac{1}{T_k} - \frac{1}{298.15}\right)\right], \tag{55}$$

where $k_{0,i}$ is the reaction rate constant at 298.15 K, E_i [J·mol^{-1}] is the apparent activation energy, and R is universal gas constant (8.314 J·K^{-1}· mol^{-1}). (The relation between rate constant and apparent activation energy for the dissolution reaction is given as

$$\ln k = -\frac{E}{RT_k} + \ln \eta_A, \tag{56}$$

where η_A is pre-exponential factor. E can be obtained by fitting the data $\ln k$ versus $-1/(RT_k)$, and the slope is E.)

For calcite dissolution (Palandri and Kharaka, 2004), the $k_{0,i}$ for acid, neutral and carbonate kinetic mineral mechanisms are, respectively, $10^{-0.3}$, $10^{-5.81}$ and $10^{-3.48}$. The activation energies are 14400, 23500 and 35400 J · mol^{-1} for these three mechanisms, respectively. The exponents for acid (a_{H^+}) and carbonate (p_{CO_2}) kinetic mechanisms are both 1.0. More data on other kinetic reactions can be found in Palandri and Kharaka (2004) and Hellevang et al. (2013). In some simplified models for GCS process, the detailed information on different reaction mechanisms is not considered. For instance, results from Smith et al. (2013) suggest that when pH variation is relatively small (e.g., pH ranges from 4 to 6), which is common at the CO_2 storage site (Emberley et al., 2005; Raistrick et al., 2006), the carbonate kinetic rate can be assumed to be independent of either pH or p_{CO_2}, and the kinetic reaction rate is (Berner and Morse, 1974; Sjöberg, 1976; Wang et al., 2016)

$$r_k = (1 - I_S)\mathcal{A}_s V \mathcal{K}. \tag{57}$$

In Smith et al. (2013), the $\mathcal{K}$ is $10^{-5.38}$ for calcite and $10^{-6.57}$ for dolomite, and the $\mathcal{A}_s$ ranges from 0.65 to 4 [10^6 m^{-1}]. Vialle et al. (2014) use $\mathcal{A}_s = 0.0469$ [10^6 m^{-1}] and $\mathcal{K} = 10^{-4.21}$ [mol·m^{-2}s^{-1}].

C. Van Genuchten Model

Van Genuchten model is employed to describe the capillary pressure and relative permeabilities of liquid brine and gaseous CO_2-rich phases (McWhorter and Sunada, 1990). The retention curve is given as

$$S_{le}(p_c) = \begin{cases} 1, p_c < 0 \\ \frac{1}{[1+(\sqrt{\frac{\kappa\bar{\phi}}{\kappa_g\phi}}\alpha_p p_c)^{n_p}]^{m_p}}, p_c \geq 0. \end{cases} \tag{58}$$

where, $\bar{\phi}$ and κ_g are mean porosity and geometric mean intrinsic permeability, respectively, $m_p = 1 - 1/n_p$, α_p [bar^{-1}] is scaling parameter for the retention curve, and S_{le} [-] is the effective saturation of brine phase. S_{le} is given as

$$S_{le} = \begin{cases} 1, \ S_l > 1 - S_{gr}; \\ \frac{S_l - S_{lr}}{1 - S_{lr} - S_{gr}}, \ S_{lr} \leq S_l \leq 1 - S_{gr}; \\ 0, \ S_l < S_{lr}, \end{cases} \tag{59}$$

where, S_{lr} [-] and S_{gr} [-] are the effective saturations of brine and gas phases. The Leverett J-function has been employed to describe entry pressure as a function of the porosity and permeability of the porous medium (Juanes et al., 2006; Plug and Bruining, 2007; Krevor et al., 2011, 2015), and thus each grid block has its own retention curve, scaled from a reference curve for the geometric mean permeability and mean porosity.

The relative permeabilities for liquid brine and gaseous CO_2-rich phases are, respectively, given as

$$\kappa_{rl} = \kappa_{rlm} \cdot (S_{le})^{\epsilon_p}[1 - (1 - S_{le}^{1/m_p})^{m_p}]^2 \tag{60}$$

and

$$\kappa_{rg} = \kappa_{rgm} \cdot (1 - S_{le})^{\gamma_p}(1 - S_{le}^{1/m_p})^{2m_p}, \tag{61}$$

where, κ_{rlm}, κ_{rgm}, ϵ_p, γ_p are the scaling parameters.

References

Berner, R.A., Morse, J.W., 1974. Dissolution kinetics of calcium carbonate in sea water; IV, Theory of calcite dissolution. American Journal of Science doi:10.2475/ajs.274.2.108.

Cao, H., 2002. Development of techniques for general purpose simulators. Ph.D. thesis. Stanford University Stanford, CA.

Carman, P.G., 1997. Fluid flow through granular beds. Chemical Engineering Research and Design doi:10.1016/s0263-8762(97)80003-2.

Carrera, J., Saaltink, M.W., Soler-Sagarra, J., Wang, J., Valhondo, C., 2022. Reactive transport: a review of basic concepts with emphasis on biochemical processes. Energies 15, 925.

Carrera, J., Vázquez-Suñé, E., Castillo, O., Sánchez-Vila, X., 2004. A methodology to compute mixing ratios with uncertain end-members. Water Resources Research doi:10.1029/2003WR002263.

Chadwick, A., Arts, R., Bernstone, C., May, F., Thibeau, S., Zweigel, P., 2008. Best practice for the storage of CO2 in saline aquifers. Halstan & Co. Ltd, Amersham .

Chen, Z., Huan, G., Ma, Y., 2006. Computational methods for multiphase flows in porous media (Vol. 2).

Elenius, M.T., Nordbotten, J.M., Kalisch, H., 2012. Effects of a capillary transition zone on the stability of a diffusive boundary layer. IMA Journal of Applied Mathematics (Institute of Mathematics and Its Applications) doi:10.1093/imamat/hxs054.

Emberley, S., Hutcheon, I., Shevalier, M., Durocher, K., Mayer, B., Gunter, W.D., Perkins, E.H., 2005. Monitoring of fluid-rock interaction and CO2 storage through produced fluid sampling at the Weyburn CO2-injection enhanced oil recovery site, Saskatchewan, Canada. Applied Geochemistry doi:10.1016/j.apgeochem.2005.02.007.

EU GeoCapacity, 2009. Assessing european capacity for geological storage of carbon dioxide, wp2 report: Storage capacity URL: http://www.geology.cz/geocapacity/publications.

Flemisch, B., Darcis, M., Erbertseder, K., Faigle, B., Lauser, A., Mosthaf, K., Müthing, S., Nuske, P., Tatomir, A., Wolff, M., Helmig, R., 2011. Dumux: Dune for multi-phase,component,scale,physics,... flow and transport in porous media. Advances in Water Resources 34, 1102 – 1112. URL: http://www.sciencedirect.com/science/article/pii/S030917081100056X, doi:https://doi.org/10.1016/j.advwatres.2011.03.007. new Computational Methods and Software Tools.

Forster, A., Norden, B., Zinck-Jørgensen, K., Frykman, P., Kulenkampff, J., Spangenberg, E., Erzinger, J., Zimmer, M., Kopp, J., Borm, G., et al., 2006. Baseline characterization of the co2sink geological storage site at ketzin, germany. Environmental Geosciences 13, 145–161.

Gasda, S.E., Nordbotten, J.M., Celia, M.A., 2012. Application of simplified models to CO 2 migration and immobilization in large-scale geological systems. International Journal of Greenhouse Gas Control doi:10.1016/j.ijggc.2012.03.001.

Gaus, I., Audigane, P., André, L., Lions, J., Jacquemet, N., Durst, P., Czernichowski-Lauriol, I., Azaroual, M., 2008. Geochemical and solute transport modelling for co2 storage, what to expect from it? International journal of greenhouse gas control 2, 605–625.

Golfier, F., Zarcone, C., Bazin, B., Lenormand, R., Lasseux, D., Quintard, M., 2002. On the ability of a Darcy-scale model to capture wormhole formation during the dissolution of a porous medium. Journal of Fluid Mechanics doi:10.1017/S0022112002007735.

Hao, Y., Smith, M., Sholokhova, Y., Carroll, S., 2013. CO2-induced dissolution of low permeability carbonates. Part II: Numerical modeling of experiments. Advances in Water Resources doi:10.1016/j.advwatres.2013.09.009.

Hao, Y., Sun, Y., Nitao, J., 2012. Overview of nuft: A versatile numerical model for simulating flow and reactive transport in porous media. Groundwater Reactive Transport Models , 212–239.

Helgeson, H.C., 1968. Evaluation of irreversible reactions in geochemical processes involving minerals and aqueous solutions-I. Thermodynamic relations. Geochimica et Cosmochimica Acta doi:10.1016/0016-7037(68)90100-2.

Helgeson, H.C., Garrels, R.M., MacKenzie, F.T., 1969. Evaluation of irreversible reactions in geochemical processes involving minerals and aqueous

511 solutions-II. Applications. Geochimica et Cosmochimica Acta doi:10.1016/0016-7037(69)90127-6.

512 Hellevang, H., Pham, V.T., Aagaard, P., 2013. Kinetic modelling of co2–water–rock interactions. International Journal of Greenhouse Gas Control
513 15, 3–15.

514 Hommel, J., Coltman, E., Class, H., 2018. Porosity–Permeability Relations for Evolving Pore Space: A Review with a Focus on (Bio-)geochemically
515 Altered Porous Media. doi:10.1007/s11242-018-1086-2.

516 Jiang, Y., 2008. Techniques for modeling complex reservoirs and advanced wells. Ph.D. thesis. Stanford University Stanford, CA, USA.

517 Johnson, J.W., Nitao, J.J., Morris, J.P., 2005. Reactive transport modeling of cap-rock integrity during natural and engineered co2 storage. Carbon
518 dioxide capture for storage in deep geologic formations 2, 787.

519 Journel, A., Huijbregts, C., 1976. Mining geostatistics.

520 Juanes, R., Spiteri, E.J., Orr, F.M., Blunt, M.J., 2006. Impact of relative permeability hysteresis on geological CO2 storage. Water Resources
521 Research doi:10.1029/2005WR004806.

522 Kim, J., Sonnenthal, E., Rutqvist, J., 2015. A sequential implicit algorithm of chemo-thermo-poro-mechanics for fractured geothermal reservoirs.
523 Computers & Geosciences 76, 59–71.

524 Kozeny, J., 1927. Uber kapillare leitung des wassers im boden. Sitzungsber Akad. Wiss., Wien .

525 Krevor, S., Blunt, M.J., Benson, S.M., Pentland, C.H., Reynolds, C., Al-Menhali, A., Niu, B., 2015. Capillary trapping for geologic carbon dioxide
526 storage - From pore scale physics to field scale implications. International Journal of Greenhouse Gas Control doi:10.1016/j.ijggc.2015.
527 04.006.

528 Krevor, S.C., Pini, R., Li, B., Benson, S.M., 2011. Capillary heterogeneity trapping of CO2 in a sandstone rock at reservoir conditions. Geophysical
529 Research Letters doi:10.1029/2011GL048239.

530 Langmuir, D., 1996. Aqueous Environmental Geochemistry. Prentice Hall, 1 edition.

531 Lasaga, A.C., 2014. Kinetic theory in the earth sciences. Princeton University Press. doi:10.5860/choice.36-4499.

532 Leal, A.M., Blunt, M.J., LaForce, T.C., 2013. A robust and efficient numerical method for multiphase equilibrium calculations: Application to CO2-
533 brine-rock systems at high temperatures, pressures and salinities. Advances in Water Resources doi:10.1016/j.advwatres.2013.02.006.

534 Leal, A.M.M., 2014. Computational Methods for Geochemical Modelling: Applications to Carbon Dioxide Sequestration. Ph.D. thesis. Imperial
535 College London.

536 Lei, H., Li, J., Li, X., Jiang, Z., 2016. Numerical modeling of co-injection of n2 and o2 with co2 into aquifers at the tongliao ccs site. International
537 Journal of Greenhouse Gas Control 54, 228–241.

538 Lichtner, P.C., 1985. Continuum model for simultaneous chemical reactions and mass transport in hydrothermal systems. Geochimica et Cos-
539 mochimica Acta doi:10.1016/0016-7037(85)90172-3.

540 Lie, K.A., 2019. An introduction to reservoir simulation using MATLAB/GNU Octave: User guide for the MATLAB Reservoir Simulation Toolbox
541 (MRST). Cambridge University Press.

542 Lie, K.A., Krogstad, S., Ligaarden, I.S., Natvig, J.R., Nilsen, H.M., Skaflestad, B., 2012. Open-source matlab implementation of consistent
543 discretisations on complex grids. Computational Geosciences 16, 297–322.

544 Liu, P., Zhang, T., Sun, S., 2019. A tutorial review of reactive transport modeling and risk assessment for geologic co2 sequestration. Computers
545 & Geosciences 127, 1–11.

546 Martinez, M.J., Hesse, M.A., 2016. Two-phase convective co2 dissolution in saline aquifers. Water Resources Research 52,
547 585–599. URL: https://agupubs.onlinelibrary.wiley.com/doi/abs/10.1002/2015WR017085, doi:10.1002/2015WR017085,
548 arXiv:https://agupubs.onlinelibrary.wiley.com/doi/pdf/10.1002/2015WR017085.

McWhorter, D.B., Sunada, D.K., 1990. Exact integral solutions for two-phase flow. Water Resources Research doi:10.1029/WR026i003p00399.

Morris, J.P., Hao, Y., Foxall, W., McNab, W., 2011. A study of injection-induced mechanical deformation at the in salah co2 storage project. International Journal of Greenhouse Gas Control 5, 270–280.

Nancollas, G.H., Reddy, M.M., 1971. The crystallization of calcium carbonate. II. Calcite growth mechanism. Journal of Colloid And Interface Science doi:10.1016/0021-9797(71)90363-8.

Neumann, R., Bastian, P., Ippisch, O., 2013. Modeling and simulation of two-phase two-component flow with disappearing nonwetting phase. Computational geosciences 17, 139–149.

Nordbotten, J.M., Celia, M.A., 2011. Geological storage of co2: modeling approaches for large-scale simulation, in: Geological Storage of CO 2: Modeling Approaches for Large-Scale Simulation. John Wiley and Sons.

Olivella, S., Carrera, J., Gens, A., Alonso, E., 1994. Nonisothermal multiphase flow of brine and gas through saline media. Transport in porous media 15, 271–293.

Olivella, S., Gens, A., Carrera, J., Alonso, E., 1996. Numerical formulation for a simulator (code_bright) for the coupled analysis of saline media. Engineering computations .

Palandri, J.L., Kharaka, Y.K., 2004. A compilation of rate parameters of water-mineral interaction kinetics for application to geochemical modeling. Technical Report.

Parkhurst, D.L., Appelo, C.A.J., 2013. Description of Input and Examples for PHREEQC Version 3 — A Computer Program for Speciation , Batch-Reaction , One-Dimensional Transport , and Inverse Geochemical Calculations.

Parvin, S., Masoudi, M., Sundal, A., Miri, R., 2020. Continuum scale modelling of salt precipitation in the context of co2 storage in saline aquifers with mrst compositional. International Journal of Greenhouse Gas Control 99, 103075.

Plug, W.J., Bruining, J., 2007. Capillary pressure for the sand-CO2-water system under various pressure conditions. Application to CO2 sequestration. Advances in Water Resources doi:10.1016/j.advwatres.2007.05.010.

Pruess, K., Oldenburg, C.M., Moridis, G.J., 1999. Tough2 user's guide version 2. Lawrence Berkeley National Lab. (LBNL), Berkeley, CA (United States) URL: https://www.osti.gov/biblio/751729, doi:10.2172/751729.

Raistrick, M., Mayer, B., Shevalier, M., Perez, R.J., Hutcheon, I., Perkins, E., Gunter, B., 2006. Using chemical and isotopic data to quantify ionic trapping of injected carbon dioxide in oil field brines. Environmental Science and Technology doi:10.1021/es060551a.

Riaño-Vilarrasa, V., 2012. Thermo-Hydro-Mechanical Impacts of Carbon Dioxide (CO2) Injection in Deep Saline Aquifers. Ph.D. thesis. Technical University of Catalonia.

Robinson, B.A., Viswanathan, H.S., Valocchi, A.J., 2000. Efficient numerical techniques for modeling multicomponent ground-water transport based upon simultaneous solution of strongly coupled subsets of chemical components. Advances in Water Resources 23, 307–324.

Rouson, D., Xia, J., Xu, X., 2011. Scientific software design: the object-oriented way. Cambridge University Press.

Saaltink, M.W., Ayora, C., Carrera, J., 1998. A mathematical formulation for reactive transport that eliminates mineral concentrations. Water Resources Research doi:10.1029/98WR00552.

Saaltink, M.W., Batlle, F., Ayora, C., Carrera, J., Olivella, S., 2004. Retraso, a code for modeling reactive transport in saturated and unsaturated porous media .

Saaltink, M.W., Carrera, J., Ayora, C., 2001. On the behavior of approaches to simulate reactive transport. Journal of Contaminant Hydrology doi:10.1016/S0169-7722(00)00172-8.

Saaltink, M.W., Vilarrasa, V., De Gaspari, F., Silva, O., Carrera, J., Rötting, T.S., 2013. A method for incorporating equilibrium chemical reactions into multiphase flow models for co2 storage. Advances in Water Resources 62, 431 – 441. URL: http://www.sciencedirect.com/science/

587 article/pii/S0309170813001747, doi:https://doi.org/10.1016/j.advwatres.2013.09.013. computational Methods in Geologic
588 CO2 Sequestration.
589 Sjöberg, E.L., 1976. A fundamental equation for calcite dissolution kinetics. Geochimica et Cosmochimica Acta doi:10.1016/0016-7037(76)
590 90009-0.
591 Smith, M.M., Sholokhova, Y., Hao, Y., Carroll, S.A., 2013. CO2-induced dissolution of low permeability carbonates. Part I: Characterization and
592 experiments. Advances in Water Resources doi:10.1016/j.advwatres.2013.09.008.
593 Steefel, C.I., Lasaga, A.C., 1994. A coupled model for transport of multiple chemical species and kinetic precipitation/dissolution reactions with
594 application to reactive flow in single phase hydrothermal systems. American Journal of Science doi:10.2475/ajs.294.5.529.
595 Steefel, C.I., Mäher, K., 2009. Fluid-rock interaction: A reactive transport approach, in: Reviews in Mineralogy and Geochemistry. doi:10.2138/
596 rmg.2009.70.11.
597 Steefel, C.I., Van Cappellen, P., 1990. A new kinetic approach to modeling water-rock interaction: The role of nucleation, precursors, and Ostwald
598 ripening. Geochimica et Cosmochimica Acta doi:10.1016/0016-7037(90)90003-4.
599 Tutolo, B.M., Kong, X.Z., Seyfried Jr, W.E., Saar, M.O., 2015a. High performance reactive transport simulations examining the effects of thermal,
600 hydraulic, and chemical (thc) gradients on fluid injectivity at carbonate ccus reservoir scales. International Journal of Greenhouse Gas Control
601 39, 285–301.
602 Tutolo, B.M., Luhmann, A.J., Kong, X.Z., Saar, M.O., Seyfried Jr, W.E., 2015b. Co2 sequestration in feldspar-rich sandstone: coupled evolution
603 of fluid chemistry, mineral reaction rates, and hydrogeochemical properties. Geochimica et Cosmochimica Acta 160, 132–154.
604 U.S. Department of Energy, 2012. The 2012 united states carbon utilization and storage atlas, 4th edition. Office of Fossil Energy URL: http:
605 //www.netl.doe.gov/research/coal/carbon-storage/atlasiv.
606 Vialle, S., Contraires, S., Zinzsner, B., Clavaud, J.B., Mahiouz, K., Zuddas, P., Zamora, M., 2014. Percolation of CO2-rich fluids in a limestone
607 sample: Evolution of hydraulic, electrical, chemical, and structural properties. Journal of Geophysical Research: Solid Earth doi:10.1002/
608 2013JB010656.
609 Vilarrasa, V., Bolster, D., Dentz, M., Olivella, S., Carrera, J., 2010a. Effects of co2 compressibility on co2 storage in deep saline aquifers. Transport
610 in porous media 85, 619–639.
611 Vilarrasa, V., Bolster, D., Olivella, S., Carrera, J., 2010b. Coupled hydromechanical modeling of co2 sequestration in deep saline aquifers.
612 International Journal of Greenhouse Gas Control 4, 910 – 919. URL: http://www.sciencedirect.com/science/article/pii/
613 S1750583610001039, doi:https://doi.org/10.1016/j.ijggc.2010.06.006. cO2 Storage at the EGU General Assembly 2009.
614 Wang, H., Bernabé, Y., Mok, U., Evans, B., 2016. Localized reactive flow in carbonate rocks: Core-flood experiments and network simulations.
615 Journal of Geophysical Research: Solid Earth doi:10.1002/2016JB013304.
616 Wang, Y., 2022. Numerical Modeling of Geological Carbon Sequestration: Enhanced Dissolution in Randomly Heterogeneous Media. Ph.D. thesis.
617 Technical University of Catalonia. URL: https://doi.org/10.5281/zenodo.6769788, doi:10.5281/zenodo.6769788.
618 Wang, Y., Fernàndez-Garcia, D., Sole-Mari, G., Rodríguez-Escales, P., 2022. Enhanced napl removal and mixing with engineered injection and
619 extraction. Water Resources Research 58, e2021WR031114.
620 Wheeler, J., et al., 2007. Integrated parallel and accurate reservoir simulator user's manual. Center for Subsurface Modeling, The University of
621 Texas at Austin .
622 Xu, T., Spycher, N., Sonnenthal, E., Zhang, G., Zheng, L., Pruess, K., 2011. Toughreact version 2.0: A simulator for subsurface reactive transport
623 under non-isothermal multiphase flow conditions. Computers & Geosciences 37, 763–774.
624 Xu, X., Chen, S., Zhang, D., 2006. Convective stability analysis of the long-term storage of carbon dioxide in deep saline aquifers. Advances in

625 Water Resources doi:10.1007/s11432-006-0397-z.

626 Zhang, K., Wu, Y.S., Pruess, K., et al., 2008. User's guide for TOUGH2-MP-a massively parallel version of the TOUGH2 code. Technical Report.
627 Ernest Orlando Lawrence Berkeley National Laboratory.

628 Zhang, W., Li, Y., Omambia, A.N., 2011. Reactive transport modeling of effects of convective mixing on long-term co2 geological storage in
629 deep saline formations. International Journal of Greenhouse Gas Control 5, 241 – 256. URL: http://www.sciencedirect.com/science/
630 article/pii/S1750583610001568, doi:https://doi.org/10.1016/j.ijggc.2010.10.007.

List of Figures

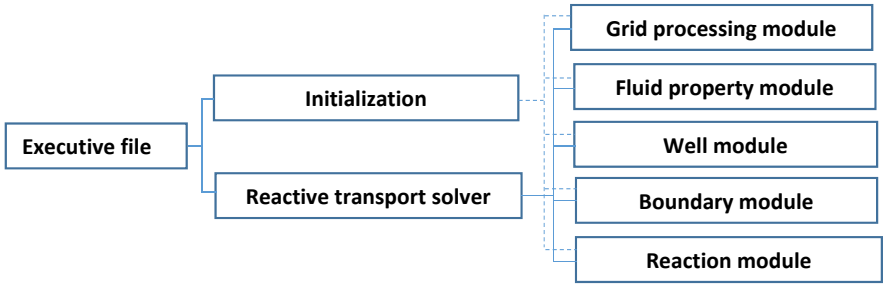

Figure 1: Code architecture; detailed implementation of the modules is given Table 1.

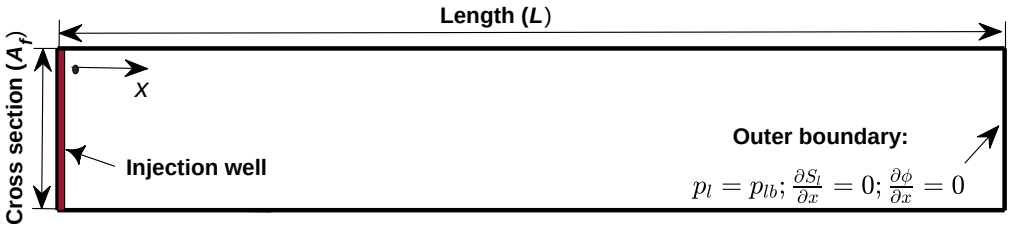

Figure 2: Setup design.

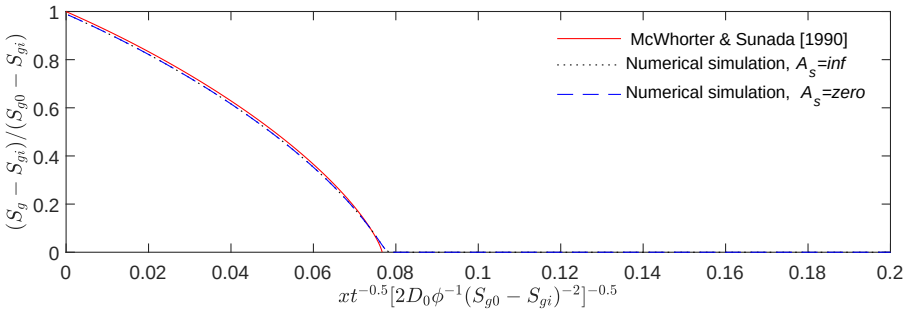

Figure 3: Comparison between the theoretical result by McWhorter and Sunada (1990) and the numerical results; initial gas pressure $p_g^i = 145[bar]$.

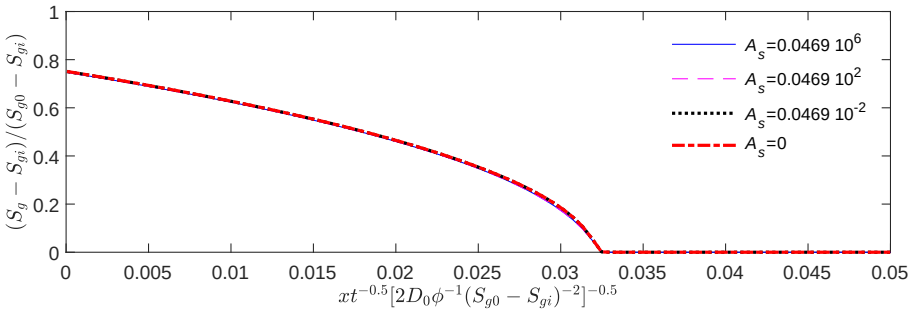

Figure 4: Comparison of the effect of reaction rate on saturation; initial gas pressure $p_g^i = 10[bar]$.

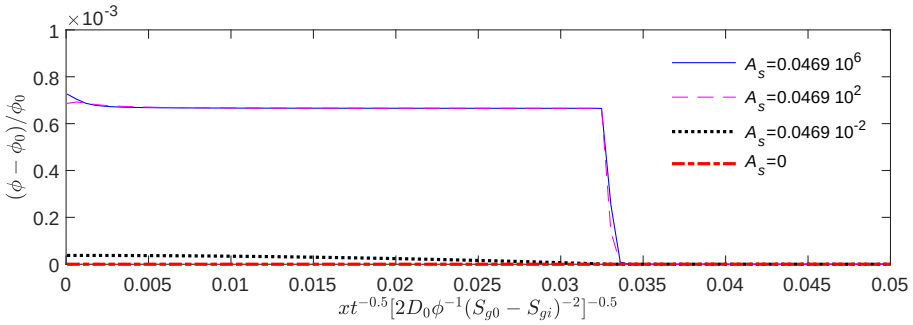

Figure 5: Comparison of the effect of reaction rate on porosity, ϕ; initial gas pressure $p_g^i = 10[bar]$.

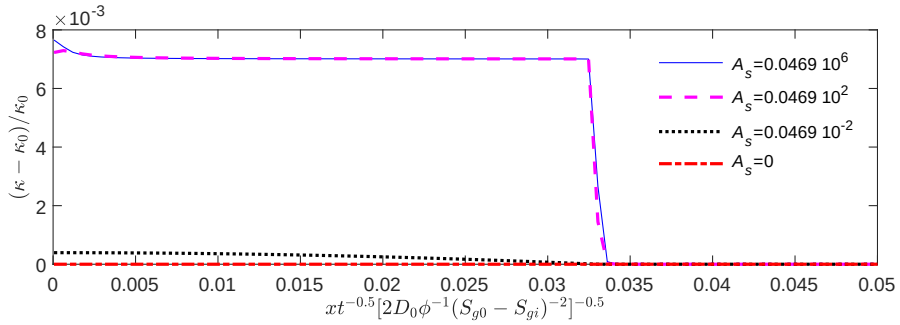

Figure 6: Comparison of the effect of reaction rate on permeability, κ; intial gas pressure $p_g^i = 10[bar]$.

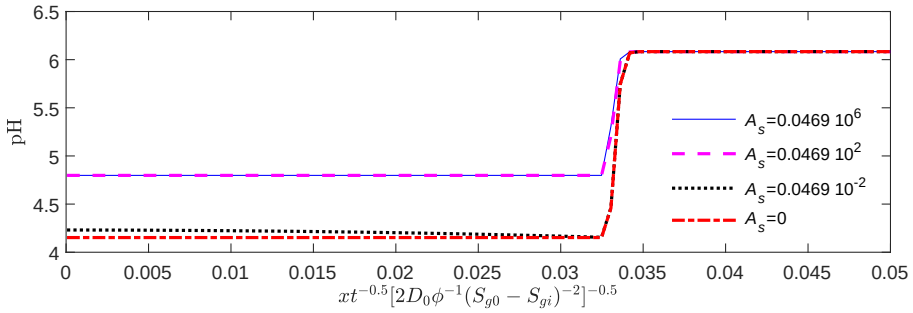

Figure 7: Comparison of the effect of reaction rate on pH; initial gas pressure $p_g^i = 10[bar]$.

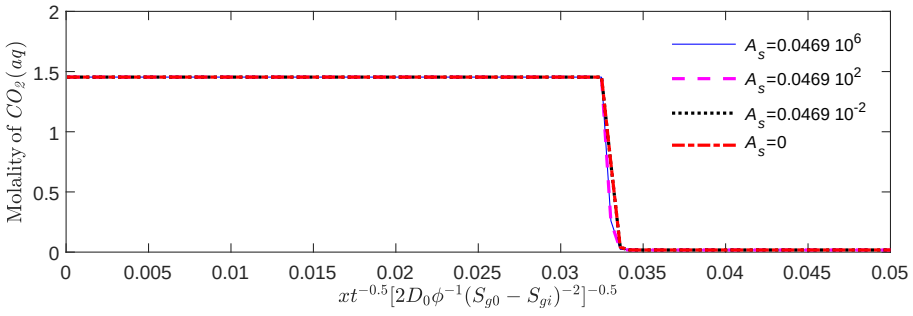

Figure 8: Comparison of the effect of reaction rate on molality of $CO_2(aq)$; initial gas pressure $p_g^i = 10[bar]$.

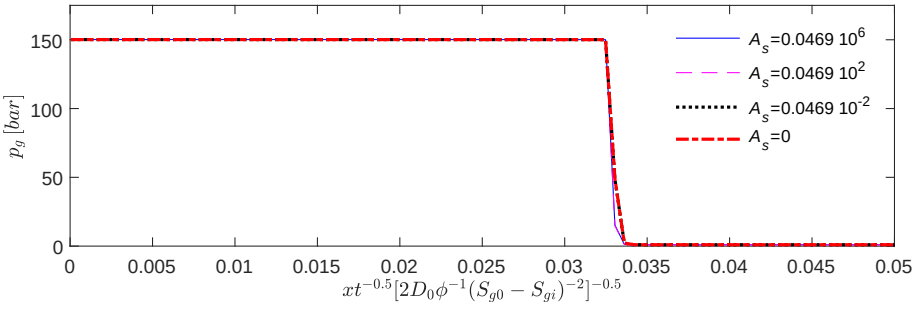

Figure 9: Comparison of the effect of reaction rate on gas pressure, p_g; initial gas pressure $p_g^i = 10[bar]$.

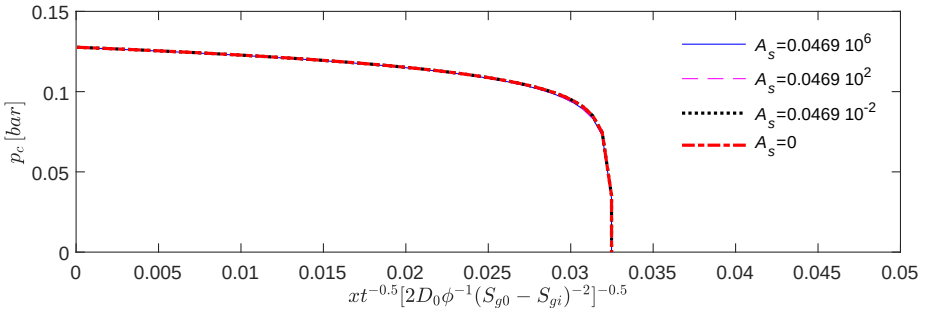

Figure 10: Comparison of the effect of reaction rate on capillary pressure, p_c; initial gas pressure $p_g^i = 10[bar]$.

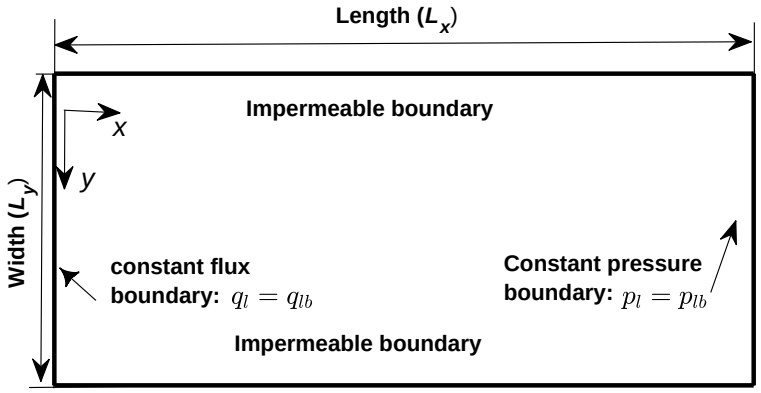

Figure 11: Setup design.

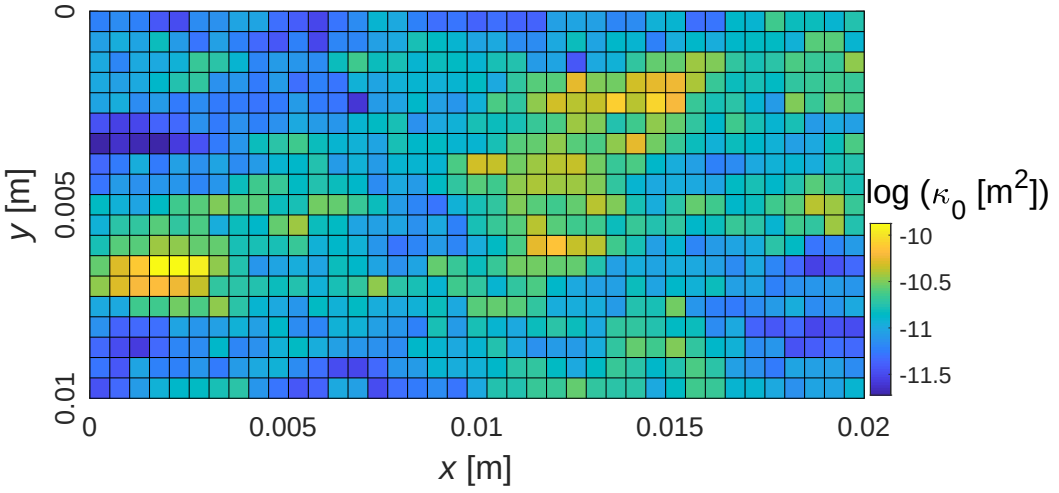

Figure 12: Initial distribution of log permeability ($\log \kappa_0$), of which the variance is 1.0.

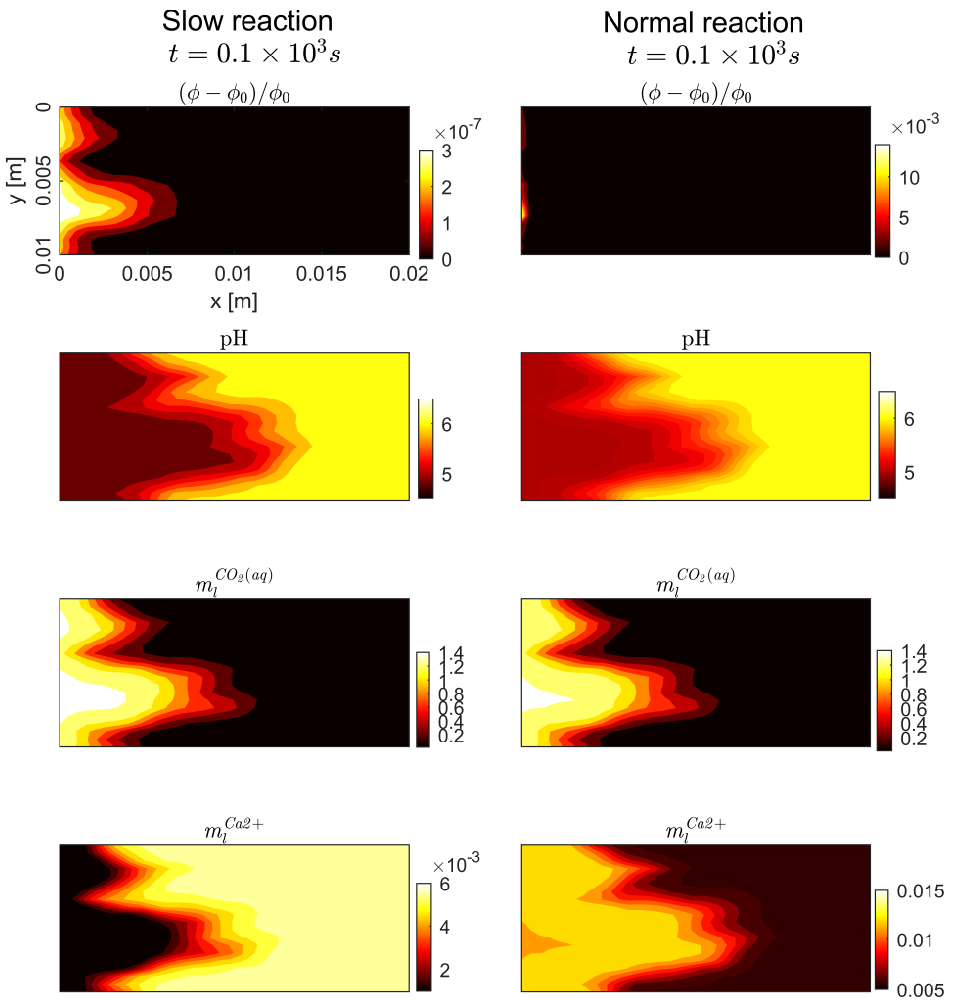

Figure 13: Distributions of porosity change ($(\phi - \phi_0)/\phi_0$), pH, molality of $CO_2(aq)$ ($m_l^{CO_2(aq)}$) and molality of Ca^{2+} ($m_l^{Ca^{2+}}$) in the field with $(\sigma_Y^0)^2 = 1$; the left column lists the results for the simulation with slow reaction, while the right column lists the results for the simulation with normal reaction; the simulation time is 0.1×10^3[s].

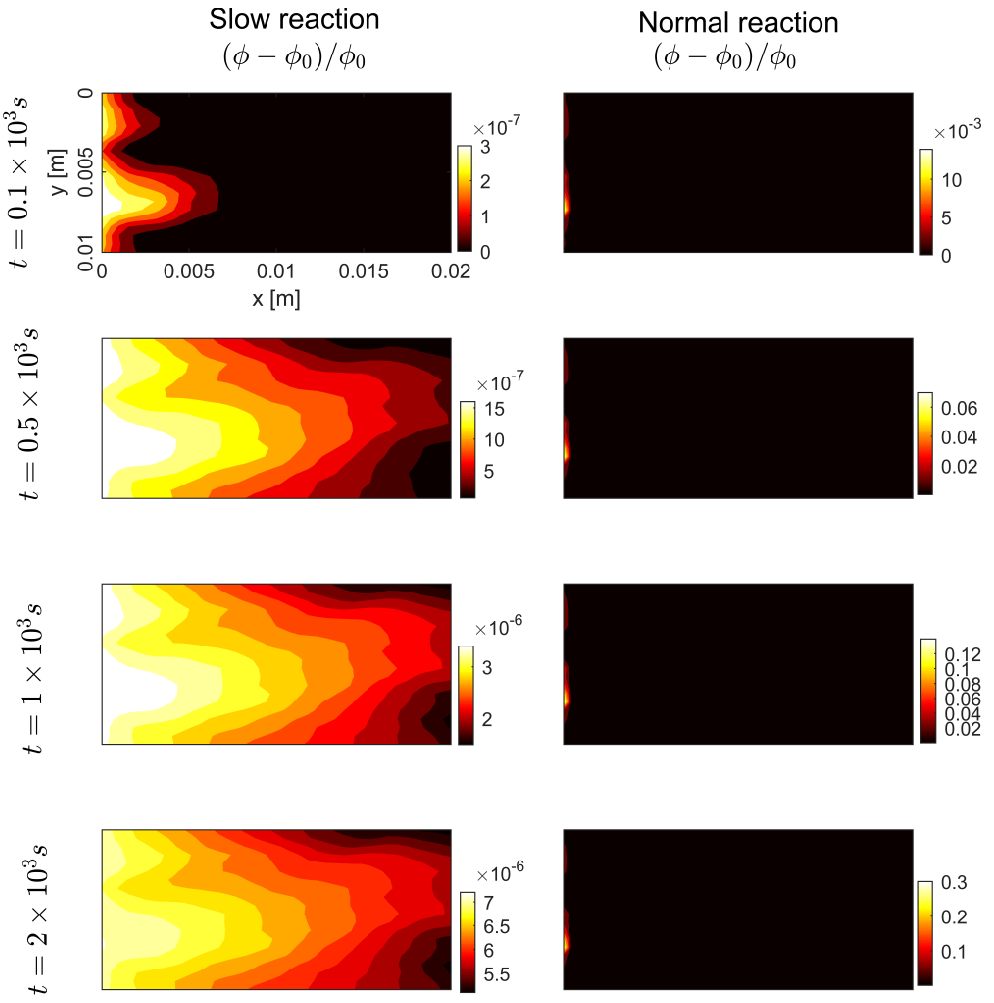

Figure 14: Temporal development of partial erosion, $(\phi - \phi_0)/\phi_0$ in the field with $(\sigma_Y^0)^2 = 1$; the left column lists the results for the simulation with slow reaction, while the right column lists the results for the simulation with normal reaction.

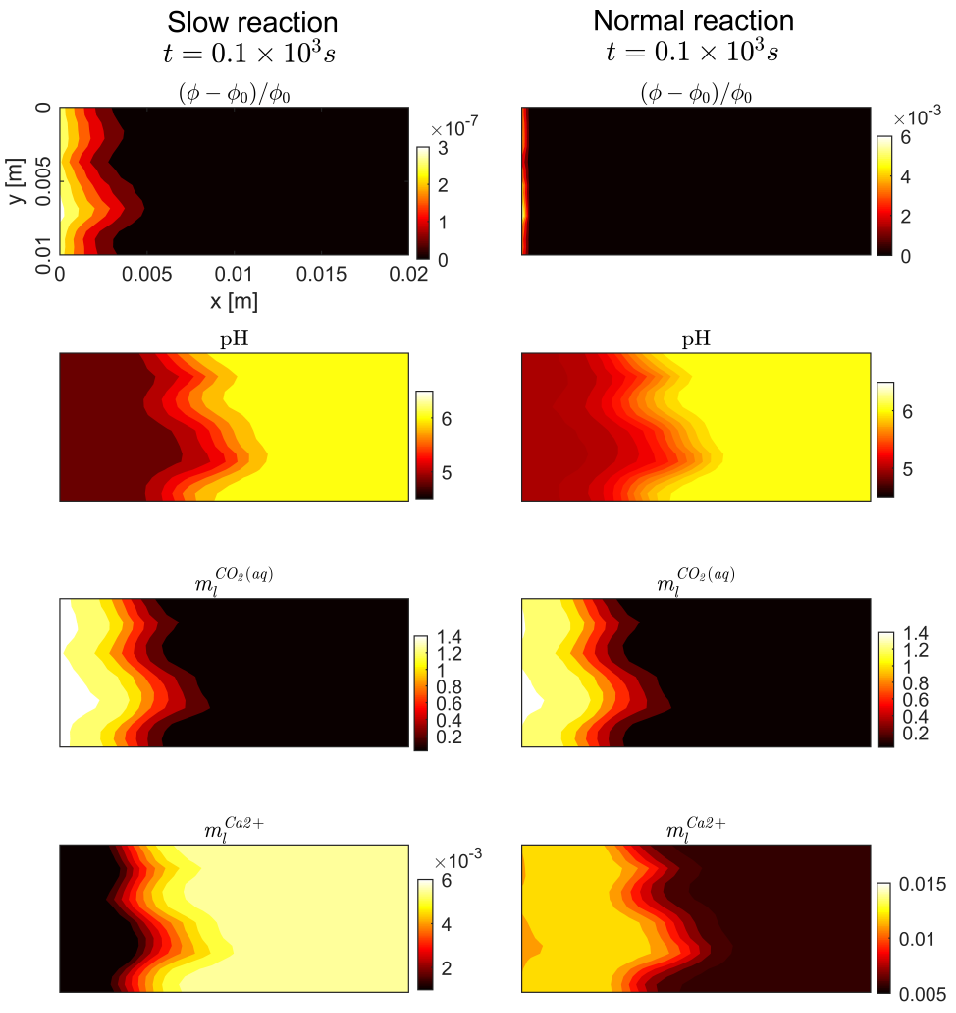

Figure 15: Distributions of porosity change ($(\phi-\phi_0)/\phi_0$), pH, molality of $CO_2(aq)$ ($m_l^{CO_2(aq)}$) and molality of Ca^{2+} ($m_l^{Ca^{2+}}$) in the field with $(\sigma_Y^0)^2 = 0.1$; the left column lists the results for the simulation with slow reaction, while the right column lists the results for the simulation with normal reaction; the simulation time is 0.1×10^3[s].

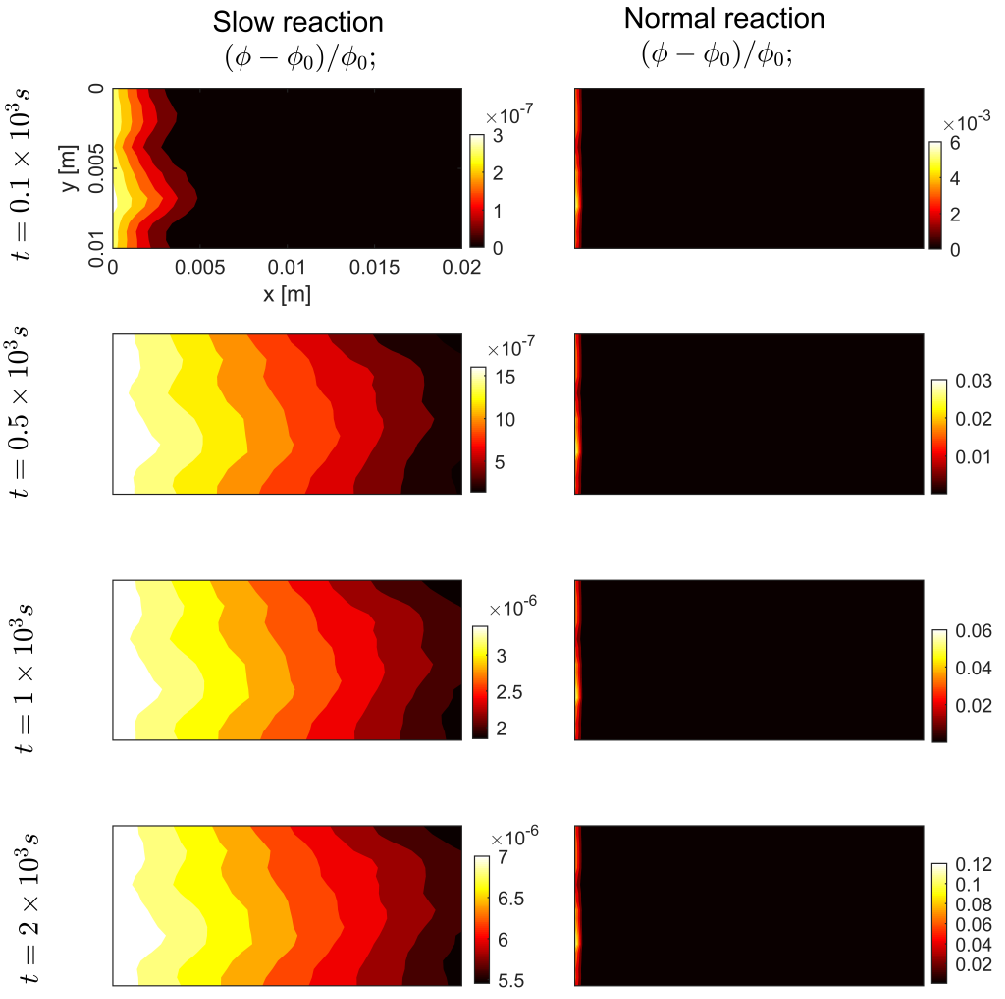

Figure 16: Temporal development of partial erosion, $(\phi - \phi_0)/\phi_0$ in the field with $(\sigma_Y^0)^2 = 0.1$; the left column lists the results for the simulation with slow reaction, while the right column lists the results for the simulation with normal reaction.